Title

Tyrosine-Based Signals Regulate the Assembly of Daple·PARD3 Complex at Cell-Cell Junctions.

Journal

iScience, 23(2)

ISSN

2589-0042

Authors

Ear, Jason
Saklecha, Anokhi
Rajapakse, Navin
et al.

Publication Date

2020-02-01

DOI

10.1016/j.isci.2020.100859

Peer reviewed

iScience

CellPress

Article

Tyrosine-Based Signals Regulate the Assembly of Daple•PARD3 Complex at Cell-Cell Junctions

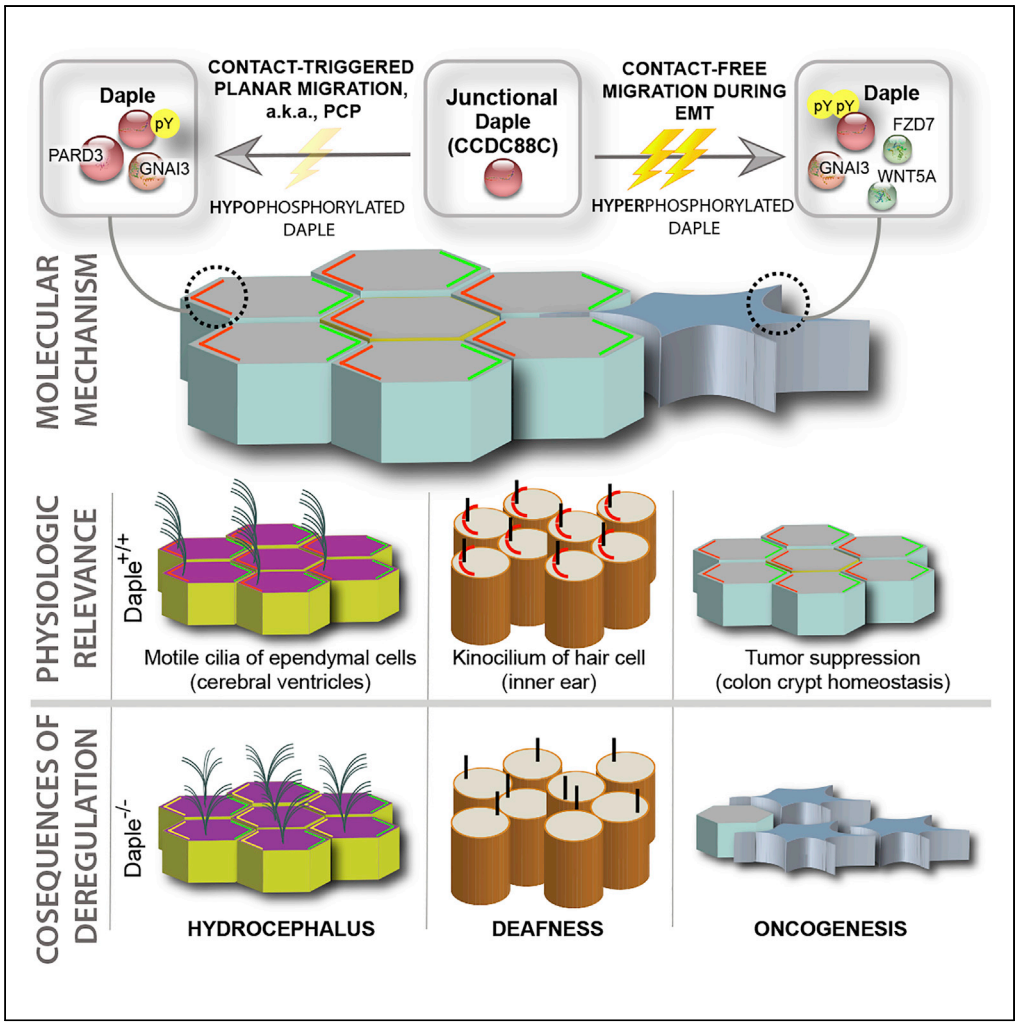

Jason Ear, Anokhi Saklecha, Navin Rajapakse, Julie Choi, Majid Ghassemian, Irina Kufareva, Pradipta Ghosh

jaear@ucsd.edu (J.E.)
prghosh@ucsd.edu (P.G.)

HIGHLIGHTS

Daple localizes to cell junction, regulates planar cell migration

Localization requires Daple's C-terminal PDZ-binding motif (PBM)

The PBM binds a PDZ module of the polarity determinant PARD3

The Daple•PARD3 interaction is regulated by tyrosine-based signals

Ear et al., iScience *23*, 100859
February 21, 2020
https://doi.org/10.1016/j.isci.2020.100859

iScience

CellPress

Article

Tyrosine-Based Signals Regulate the Assembly of Daple•PARD3 Complex at Cell-Cell Junctions

Jason Ear,[1,*] Anokhi Saklecha,[1] Navin Rajapakse,[1] Julie Choi,[1] Majid Ghassemian,[2] Irina Kufareva,[3] and Pradipta Ghosh[1,4,5,6,7,*]

SUMMARY

Polarized distribution of organelles and molecules inside a cell is vital for a range of cellular processes and its loss is frequently encountered in disease. Polarization during planar cell migration is a special condition in which cellular orientation is triggered by cell-cell contact. We demonstrate that the protein Daple (CCDC88C) is a component of cell junctions in epithelial cells which serves like a cellular "compass" for establishing and maintaining contact-triggered planar polarity. Furthermore, these processes may be mediated through interaction with the polarity regulator PARD3. This interaction, mediated by Daple's PDZ-binding motif (PBM) and the third PDZ domain of PARD3, is fine-tuned by tyrosine phosphorylation on Daple's PBM by receptor and non-receptor tyrosine kinases, such as Src. Hypophosphorylation strengthens the interaction, whereas hyperphosphorylation disrupts it, thereby revealing an unexpected role of Daple as a platform for signal integration and gradient sensing for tyrosine-based signals within the planar cell polarity pathway.

INTRODUCTION

Epithelial cell-cell adhesion and cell polarity are necessary for proper cell function and tissue organization (Rodriguez-Boulan and Macara, 2014). Cells along an epithelium are connected together through various junctional complexes (tight junction, adherens junctions, desmosomes, and gap junctions), which are essential in establishing the apical and basolateral pole of a cell (referred to as the apical-basal axis) (Farquhar and Palade, 1963). In addition to an apical-basal polarity, cells are also polarized along the plane of the epithelium, referred to as planar cell polarity (PCP) (Henderson et al., 2018). Dysregulation of these cell adhesion complexes and cell polarity can lead to maladies such as inflammatory bowel diseases, hydrocephalus, abnormal skin barrier function, and tumor initiation and progression (Bhat et al., 2018). In fact, disruption of cellular junctions is one of the first events during epithelial-to-mesenchymal transition (EMT), a phenomenon that is encountered during cancer initiation and progression (Bhat et al., 2018; Feigin and Muthuswamy, 2009). Thus, cell-cell junctions are widely believed to serve as tumor suppressors (Knights et al., 2012; Martin et al., 2011).

A typical cell junction is composed of a layer of transmembrane molecules that functions for hetero- and homotypic binding between cells and a layer of molecular scaffolds peripheral to the membrane. These scaffolds tether transmembrane molecules to key intracellular molecules such as the cytoskeleton or signaling molecules. Many of these scaffolds contain one or more PDZ domains (Post synaptic density protein [PSD95], Drosophila disc large tumor suppressor [Dlg1], and Zonula occludens-1 protein [ZO-1]), which mediate interactions with other proteins that contain a PDZ-binding motif (PBM) (Subbaiah et al., 2011). Mutations affecting PDZ•PBM interactions have exposed the importance of these junction-localized interactions in the regulation of key tumor cell phenotypes (Subbaiah et al., 2011).

Daple (CCDC88C) is a large, multi-modular PBM-containing scaffold protein (Aznar et al., 2015, 2018). First discovered in a yeast-two hybrid screen through its ability to bind to the PDZ domain on Disheveled (Dvl), Daple has emerged as a key modulator of Wnt signaling (Aznar et al., 2015; Ishida-Takagishi et al., 2012). The extreme C-terminus on Daple contains an "atypical" PBM, which we, and others, demonstrated to be necessary for the Daple•Dvl interaction (Aznar et al., 2018; Ishida-Takagishi et al., 2012; Kobayashi et al., 2005). We subsequently showed that Daple binds Gαi proteins and triggers GTPase signaling downstream of the Wnt receptor Frizzled-7 upon activation by Wnt5a; such signaling is necessary for the activation of the

[1]Department of Cellular and Molecular Medicine, University of California San Diego, 9500 Gilman Drive (MC 0651), George E. Palade Bldg, Rm 331-333, La Jolla, CA 92093, USA

[2]Department of Chemistry and Biochemistry, University of California San Diego, La Jolla, CA 92093, USA

[3]Skaggs School of Pharmacy and Pharmaceutical Sciences, University of California San Diego, La Jolla, CA 92093, USA

[4]Department of Medicine, University of California San Diego, 9500 Gilman Drive (MC 0651), George E. Palade Bldg, Rm 331-333, La Jolla, CA 92093, USA

[5]Rebecca and John Moore Comprehensive Cancer Center, University of California San Diego, La Jolla, CA 92093, USA

[6]Veterans Affairs Medical Center, La Jolla, CA, USA

[7]Lead Contact

*Correspondence: jaear@ucsd.edu (J.E.), prghosh@ucsd.edu (P.G.)

https://doi.org/10.1016/j.isci.2020.100859

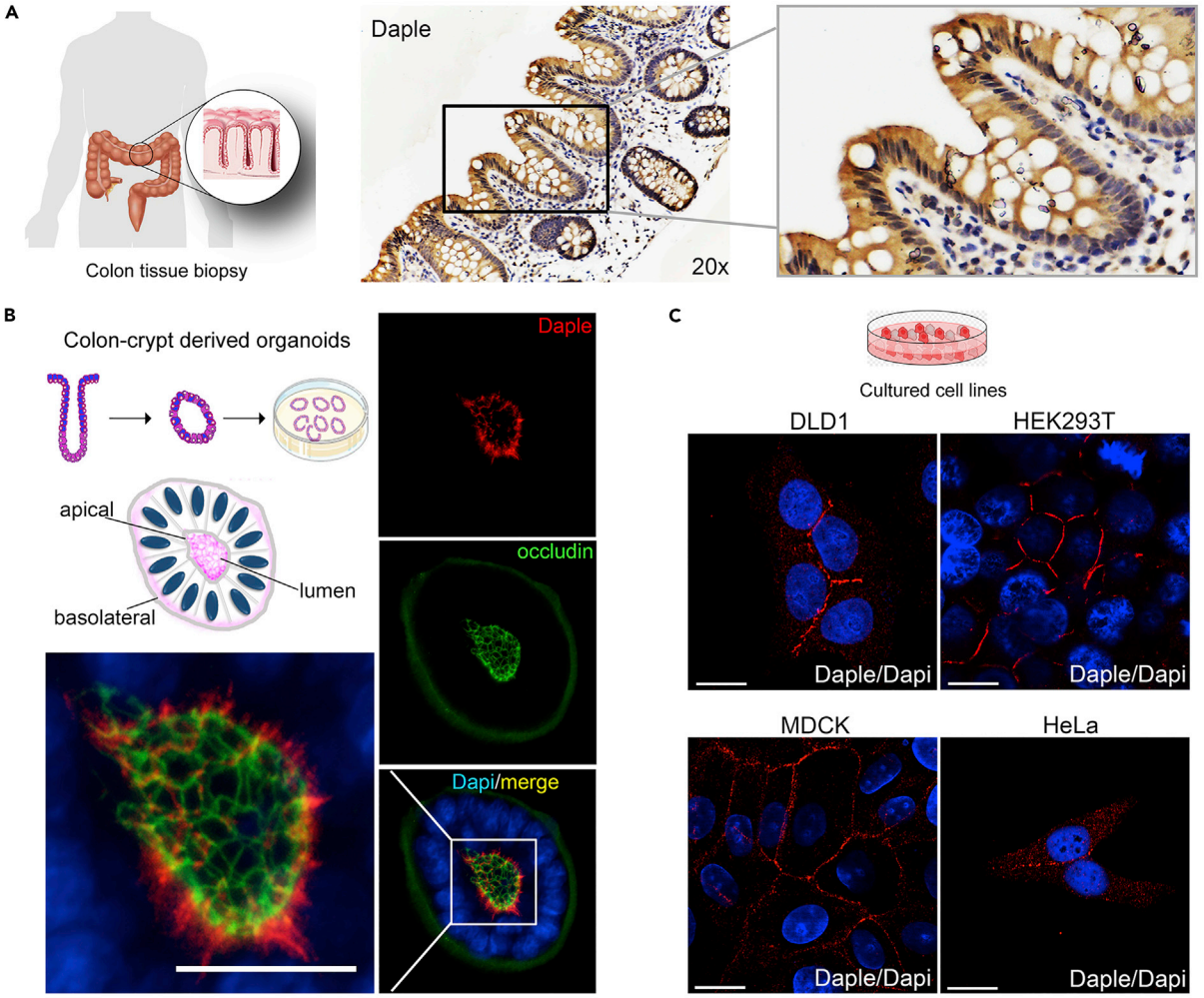
A
Colon tissue biopsy
Daple
20x
B
Colon-crypt derived organoids
apical
lumen
basolateral
Daple
occludin
Dapi/merge
C
Cultured cell lines
DLD1
HEK293T
Daple/Dapi
Daple/Dapi
MDCK
HeLa
Daple/Dapi
Daple/Dapi
D
occludin
Daple
Dapi/merge
Fluorescence (A.U.)
Distance in pixels
occludin
Daple
β-catenin
Daple
Dapi/merge
Fluorescence (A.U.)
Distance in pixels
β-catenin
Daple

Figure 1. Daple Localizes to the Cell-Cell Junctions in Polarized Epithelial Cells

(A) Immunohistochemistry staining on human colon biopsy sections showed that Daple is highly expressed in the colon epithelium.

(B) Human colon-derived organoids were fixed and stained for Daple (*red*) and occludin (*green*) and analyzed by confocal microscopy. A representative image is shown; scale bar, 25 μm.

(C) Various epithelial cell lines (DLD1, HEK293T, MDCK, and HeLa) were fixed, stained for Daple (red) and nucleus (Dapi), and analyzed by confocal microscopy. Scale bar, 10 μm.

(D) MDCK cells were fixed, stained for Daple (*red*) and either the tight junction marker, occludin (*green, top*) or the adherens junction maker, β-catenin (*green, bottom*), and analyzed by confocal imaging. Scale bar, 10 μm. *Left*: Representative images are shown. *Right*: RGB profile plot of indicated region is shown.

β-catenin-independent Wnt signaling pathway (a.k.a. non-canonical Wnt signaling). More recently, we showed Daple-dependent Wnt signaling is also shaped by Akt and multiple tyrosine kinases (TKs); in each case, phosphorylation of Daple by these kinases impacted its localization and signaling (Aznar et al., 2015, 2017, 2018). We also showed that Daple has two opposing roles during colorectal cancer (CRC) progression; much like the non-canonical Wnt pathway, Daple acts as a tumor suppressor in the normal epithelium and early during cancer initiation, but it serves as a potent trigger for EMT and tumor cell invasion later during cancer dissemination. How does one protein serve two seemingly opposing roles, and how its tumor-suppressive and pro-metastatic functions are segregated remains poorly understood.

Here we show that Daple's functions are tightly regulated by spatial segregation, which is dictated by its interactome and the context, i.e., cell type and key phosphomodifications that are triggered by growth factors. Such fine-tuned regulation of Daple's subcellular localization and its interactome offers insight into Daple's dual role during cancer progression and other cell polarity-associated diseases.

RESULTS AND DISCUSSION

Daple Is Localized on Cell-Cell Junctions in Epithelial Cells and Tissues

To investigate the role of Daple in the normal colonic epithelium, we first studied the expression and subcellular localization of Daple using a previously validated antibody against its C-terminus in a variety of immunocytochemical approaches. By immunohistochemistry on formalin-fixed paraffin-embedded colon biopsies, we confirmed that Daple is indeed expressed in the epithelial lining of the human colon (Figure 1A). By immunofluorescence staining and confocal imaging of human colon-derived organoids cultured in matrigel, we determined the localization of Daple at a higher resolution; it localizes at the apical side of the epithelial cells facing the lumen, marked by the tight junction protein, occludin. Findings suggest that Daple is on the apical pole of the epithelial cells (Figure 1B). By immunofluorescence on monolayers of cultured cancer cell lines, we observed Daple at the sites of cell-cell contact (Figure 1C). In the highly polarized MDCK cells, we observe colocalization with the tight junction marker occludin as well as with the adherens junction marker, β-catenin (Figure 1D). Taken together, these findings demonstrate that a significant pool of the cytosolic protein Daple localizes to cell-cell junctions. This is in keeping with prior observations made by others using ependymal, inner ear, and MDCK cells (Siletti et al., 2017; Takagishi et al., 2017; Aznar et al., 2017; Marivin and Garcia-Marcos, 2019; Marivin et al., 2019). These findings suggest that Daple may physically associate with various junctional complexes to maintain such localization.

Daple Localizes to Cell Junctions in Well-Differentiated CRC Cells, Requires Junctional Complexes

Next, we examined the subcellular localization of Daple in several CRCs cell lines. Daple was found at cell-cell junctions in the poorly metastatic CaCo-2 cells but was predominantly cytosolic in the highly metastatic Sw480 cells (Figure S1A). The total levels of expression of Daple in both cell lines are comparable (Figure 2A), leading us to conclude that the observed differences in localization are likely due to the absence of cell junctions in Sw480 cells.

To further investigate this differential localization, we took advantage of the fact that most CRC cell lines have a mix of well-differentiated non-invasive epithelioid (henceforth, E-type) and poorly differentiated highly invasive rounded (henceforth, R-type) cells representing transition states of CRC progression (Ciasca et al., 2016). We studied two well-characterized DLD1 E-type and R-type lines (Vermeulen et al., 1995); the latter lacks the adherens junction protein, α-catenin. We chose to study this pair because loss of α-catenin has previously been shown to be associated with a poorly differentiated status of CRCs and a worse prognosis in patients (Figure S1B). Several clones of E-type and R-type cells (see Figure S1C for distinct

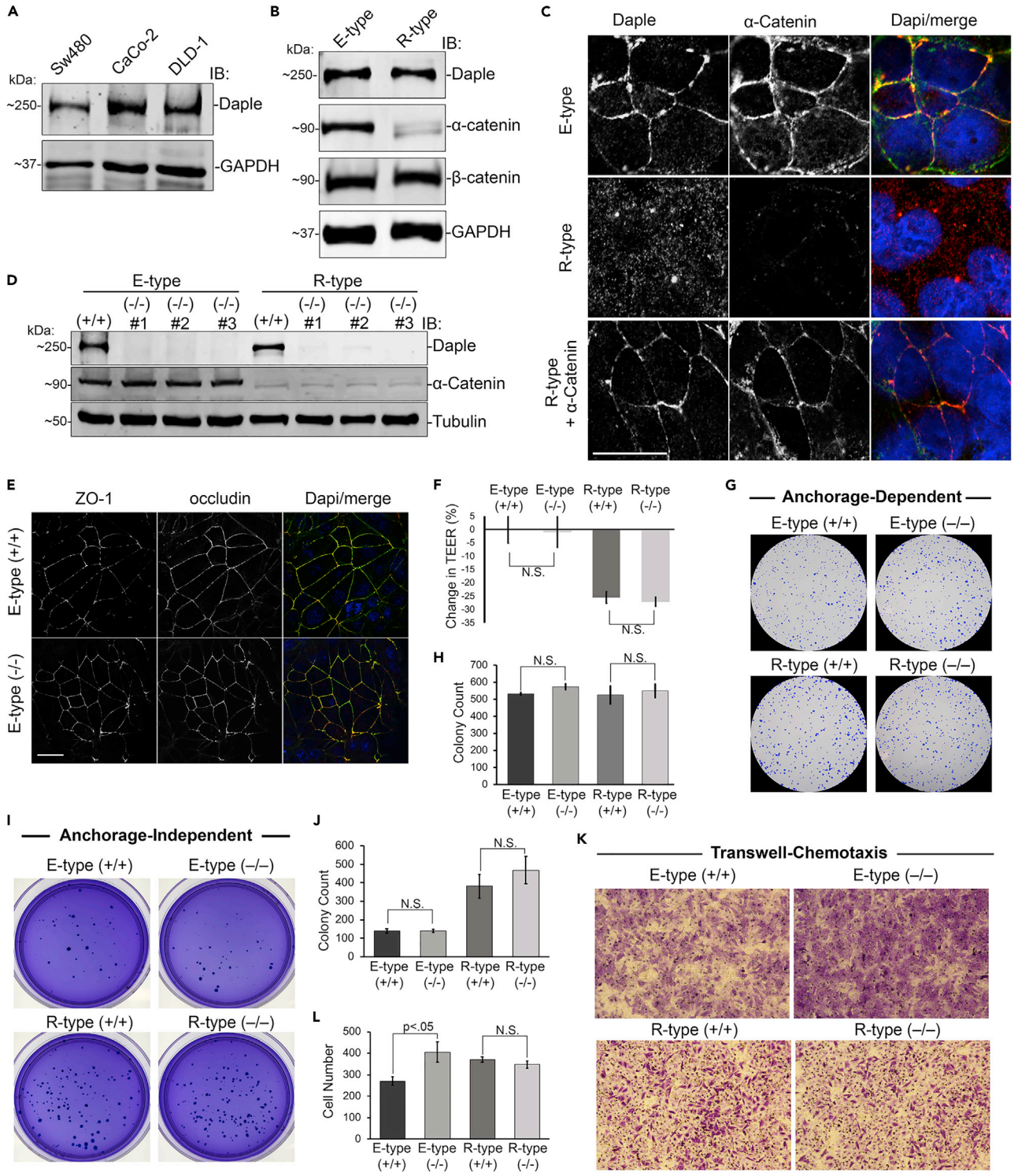

Figure 2. Depletion of Daple in the Poorly Migrating DLD1 E-type Cells versus the Highly Invasive R-type Cells Have Differential Effect on Cell Migration

(A) Immunoblot of whole-cell lysates of Sw480, CaCo-2, and DLD1 colorectal cancer cells for Daple expression.

(B) Immunoblot of whole-cell lysates of DLD1 E-type and R-type cells for Daple and α-catenin expression.

(C) DLD1 E-type, R-type, and R-type cells transiently expressing α-catenin were fixed and immunostained for Daple (*red*) and α-catenin (*green*). Scale bar, 5 μm.

Figure 2. *Continued*

(D) Immunoblot of DLD1 E-type and R-type CRISPR/Cas9 clones targeted for Daple confirming depletion.

(E) DLD1 E-type cells depleted of Daple (−/−) were stained for cell junction markers ZO-1 (*red*) and occludin (*green*); representative images are shown. Scale bar, 25 μm.

(F) Transepithelial electrical resistance (TEER) of DLD1 E-type and R-type cells depleted (−/−) or not (+/+) of Daple. Measurements are represented as percent change relative to E-type (+/+) cells.

(G and H) Anchorage-dependent colony growth assay on DLD1 E-type and R-type depleted (−/−) or not (+/+) of Daple. Bar graphs (H) show quantification of panels in (G).

(I and J) Anchorage-independent growth assay on DLD1 E-type and R-type cells depleted (−/−) or not (+/+) of Daple. Bar graphs (J) show quantification of panels in (I).

(K and L) Transwell migration assay on DLD1 E-type and R-type cells toward 2% serum. Bar graphs (L) show quantification of panels in (K). N.S. = Not significant in (F, H, J, and L).

morphology) were isolated and the loss of α-catenin in R-type cells was confirmed by immunoblotting (Figure S1D). Although both clones appear to express similar levels of Daple protein, as determined by immunoblotting (Figure 2B), localization of Daple in these cells looked as different as that previously observed between CaCo-2 and Sw480; Daple was at cell-cell junctions in the E-type cells but in the cytoplasm in R-type cells (Figure 2C). It is noteworthy that many components of cell junctions are insoluble in detergents such as Triton x-100 (Tx100) owing to their association with the cortical actin at the cell periphery. Daple was detected in Tx100-insoluble fractions in all cell types tested (Figures S2A–S2C), suggesting that regardless of its junctional localization, Daple remains associated with the actin cytoskeleton.

Next, we carried out a series of studies to dissect whether Daple's localization to cell-cell junctions is an active process of recruitment to that site or a passive consequence due to the formation of these junctions. Transient expression of α-catenin into R-type cells restored the localization of Daple at cell junctions, mimicking E-type cells (Figure 2C). Conversely, disruption of cell junctions in E-type cells by calcium depletion (using the calcium-chelator, EGTA) triggered redistribution of Daple from cell junctions to the cytoplasm (Figure S1E). Prior work showed that activation of PKC in R-type cells (using TPA, tetradecanoyl phorbol acetate) transiently restores junctions (van Hengel et al., 1997); although we too observed an increase in the localization of occludin at the junctions upon TPA treatment, Daple did not localize there (Figure S1F). These findings demonstrate that the assembly and disassembly of adherens junctions is a key determinant of Daple's localization at cell junctions. The observation that exogenous expression of α-catenin, but not TPA treatment, was sufficient to restore Daple's localization at cell junctions suggests that Daple's ability to localize to this subcellular site is an active process of recruitment that may require interactions with stable junctional structures.

Junction-Localized Daple Enables Contact-Triggered Orientation and Polarized Planar Migration

To investigate if junction-localized Daple may regulate key cellular phenotypes, we depleted Daple in the E-type and R-type cells by CRISPR/Cas9 and confirmed by immunoblotting (Figures 2D and S3A–S3C). Depletion of Daple in E-type did not alter the levels of α-catenin (Figure 2D) and did not have a discernible impact on the morphology of cell junctions, as evident by localization of the integral membrane protein occludin and the peripheral tight junction protein ZO-1 (Figure 2E). There was also no discernible impact on the functional integrity of tight junctions, i.e., regardless of Daple depletion, the paracellular permeability remained unchanged, as determined by measurements of transepithelial electrical resistance (TEER) on a confluent monolayer of cells (Figure 2F). These findings indicate that loss of Daple may be dispensable for the morphological or functional integrity of tight junctions in epithelial cells grown in confluent monolayers. Findings are also consistent with what has been reported by others for tight junctions in the blood-brain barrier or Daple −/− mice (Takagishi et al., 2017).

Because junctions are also known to serve as signaling microdomains that dictate tumor-sphere growth and cell migration (Martin et al., 2011; Wu et al., 2011; Bhat et al., 2018; Feigin and Muthuswamy, 2009; Knights et al., 2012), next we asked if these growth and motility phenotypes are impacted in Daple-depleted cells. Under the conditions tested, we observed no significant changes in growth either in anchorage-dependent or in anchorage-independent colony formation assays (Figures 2G–2J). When we measured the ability of these cells to migrate across a semipermeable membrane across a 0%-to-2% serum gradient, loss of Daple led to an increase in chemotaxis in the E-type but not in the R-type cells (Figures 2K and 2L), indicating that loss of junctional Daple induces gradient-responsive migration in 3 dimension (3D).

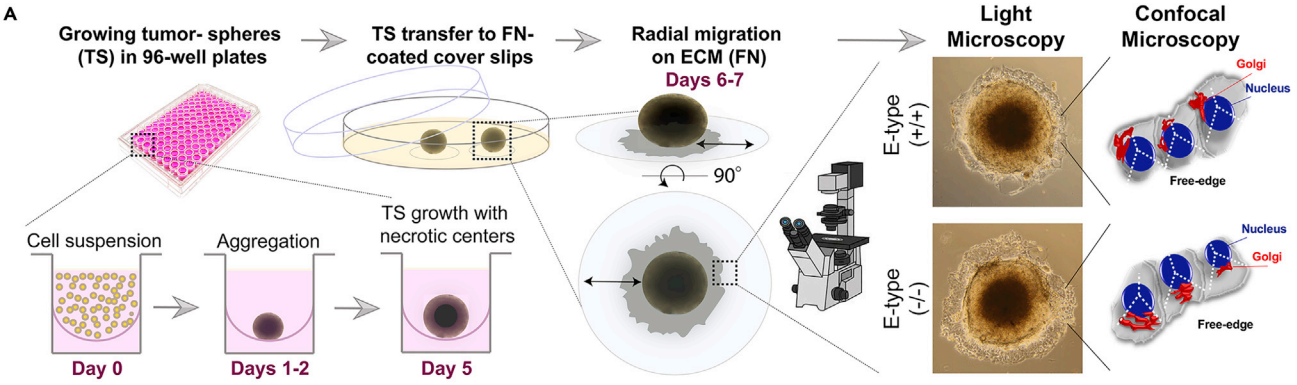
A
Growing tumor- spheres (TS) in 96-well plates
TS transfer to FN-coated cover slips
Radial migration on ECM (FN)
Days 6-7
90°
Light Microscopy
Confocal Microscopy
E-type (+/+)
E-type (-/-)
Golgi
Nucleus
Free-edge
Cell suspension
Aggregation
TS growth with necrotic centers
Day 0
Days 1-2
Day 5

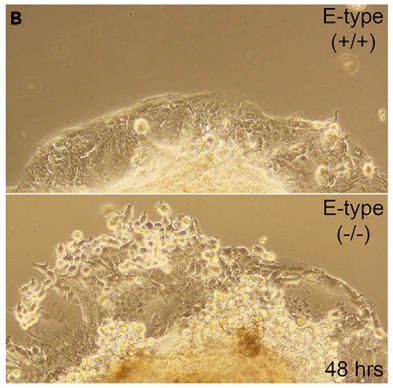
B
E-type (+/+)
E-type (-/-)
48 hrs

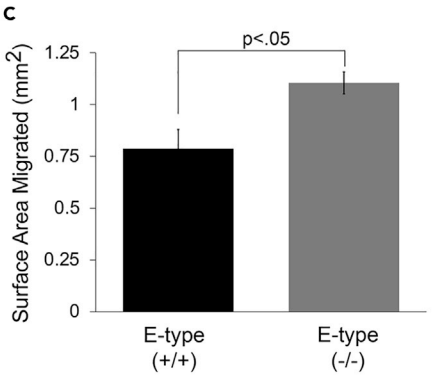
C
p<.05
Surface Area Migrated (mm2)
1.25
1
0.75
0.5
0.25
0
E-type (+/+)
E-type (-/-)

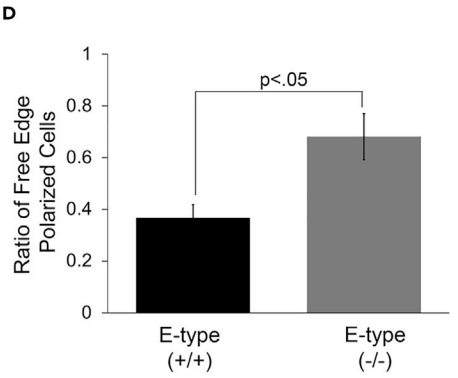
D
p<.05
Ratio of Free Edge Polarized Cells
1
0.8
0.6
0.4
0.2
0
E-type (+/+)
E-type (-/-)

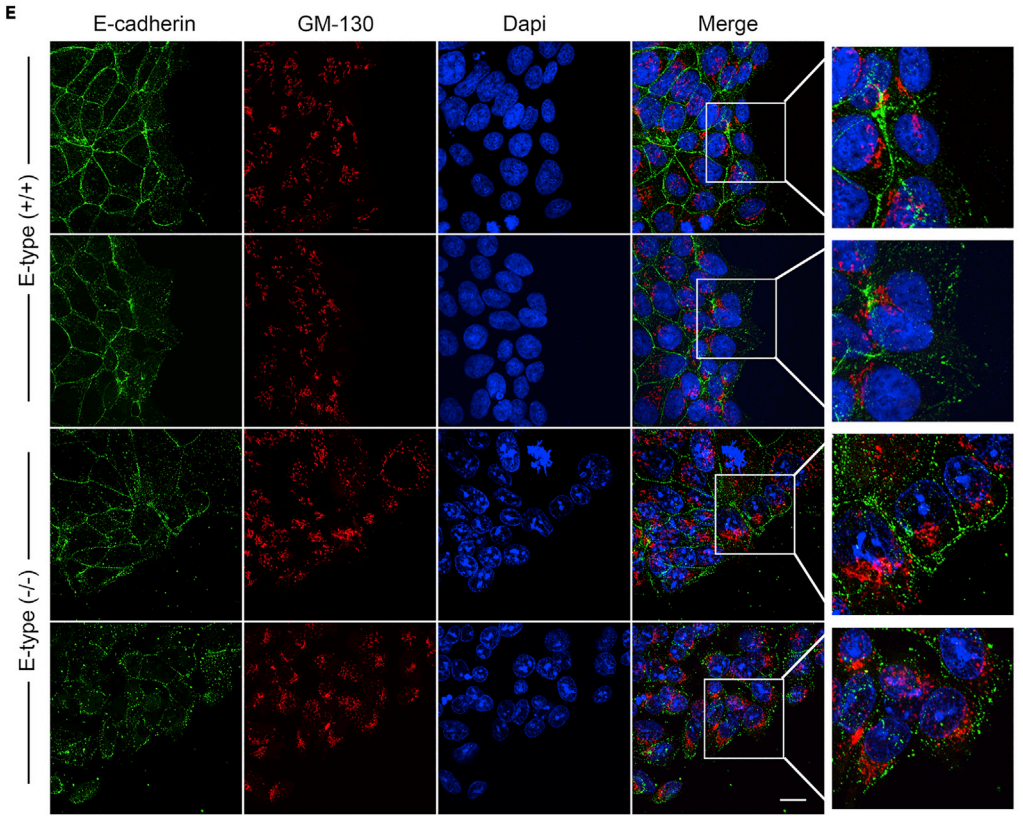
E
E-cadherin
GM-130
Dapi
Merge
E-type (+/+)
E-type (-/-)

Figure 3. Loss of Daple Affects Planar Migration of DLD1 E-type Cells

(A) Schematic of workflow for tumor spheroid growth and assessment of radial migration by light and confocal microscopy. Polarization of migrating cells was monitored by assessing the position of the Golgi (using GM-130) relative to the advancing edge and the nucleus (using DAPI).

(B) Magnified view of the edge of the tumor sphere showing radially migrating sheets of E-type (+/+) and (−/−) cells after 48 h, as visualized by light microscopy.

(C) Bar graphs show the extent of surface area of sheet-like migration in (B) Data are represented as mean ± SEM.

(D and E) Radially migrated cells, as in (C), were fixed and stained for the *bona fide* Golgi marker GM130 (*red*) and E-cadherin (*green*). The ratio of polarized cells to total cells was quantified (E). Data are represented as mean ± SEM.

Because Daple is an enhancer of non-canonical Wnt signaling (Aznar et al., 2015; Ishida-Takagishi et al., 2012; Kobayashi et al., 2005), signals that mediate the phenomenon of orderly polarized migration over 2D planes, a.k.a planar cell polarity (PCP) (Henderson et al., 2018; Takagishi et al., 2017), we asked if junction-localized Daple may impact this phenomenon. PCP is a critical tumor suppressive phenomenon that maintains homeostasis in the colon crypt by ensuring that the cells newly generated from the crypt base-localized stem cells migrate along the basement membrane (2D migration on a plane) to constantly replenish the crypt top-localized terminally differentiated surface epithelial layer, which displays a high turnover rate (Fatehullah et al., 2013; Schneeberger et al., 2018). When studying PCP in cell culture, migrating cells are typically monitored on a planar surface (Gandalovicova et al., 2016; Schmoranzer et al., 2009). Although this mode of migration is more accurately accessing front-rear polarity, many components in front-rear polarity is conserved in PCP (Gandalovicova et al., 2016). We utilized one such previously described planar cell migration model (Kramer et al., 2013) in which cells are first grown in suspension to form a compact spheroid, then transferred onto an adherent substrate and monitored by light and confocal microscopy for polarized radial migration (Figure 3A). We chose fibronectin as the substrate because it is well accepted as the matrix of choice for PCP studies (Yi et al., 2016; Dohn et al., 2013). Although no differences were observed between spheroids grown using wild-type and Daple knockout E-type cells (Figures S3D and S3E), Daple-depleted cells migrated out significantly more than wild-type cells, losing cell-cell contacts (higher birefringence in light microscopy, Figure 3B) covering a greater surface area (Figures 3B and 3C). These migrating cells also displayed a loss of cell-cell contact (marked by the adherens junction marker, E cadherin) and loss of contact-triggered orientation toward the spheroid and instead polarized toward the free edge, as determined by the relative positions of the nucleus and the Golgi body (marked by the integral membrane protein, GM130) (Nakamura et al., 1995, 1997). Compared with wild-type cells, a greater number of Daple-depleted cells positioned their Golgi away from the spheroid, indicating that cells were polarized toward the free edge, which is consistent with their observed increased motility in both 2D and 3D assays (Figures 3D and 3E). Overall, these finding implicate Daple in front-rear polarity (and presumably PCP); its loss disrupted contact-triggered orientation and migration and instead promoted contact-free scattering. Because others have implicated Daple in regulating apical-basal polarity and apical constriction in epithelial cells (Marivin et al., 2019), taken together, these findings indicate that junction-localized Daple may serve as a nexus between two types of polarity—"apical-basal" and "front-rear." Because Daple serves this role in the context of sheet-like migration of cells on a planar surface, findings suggest it regulates PCP.

Biotin Proximity Labeling Identifies Various PDZ-Proteins within Daple's Interactome

We hypothesized that junction-localized Daple may impact PCP via the coordinated regulation of signaling co-complexes that sense and respond to cell-cell contact via adherens junctions (but may not regulate tight junction integrity). To gain insights into how/why Daple localizes to the cell junctions and impacts PCP, we carried out BioID proximity labeling coupled with mass spectrometry (MS) to identify interacting proteins. We carried out these studies in both in E- and R-type cells and HEK293T cells to specifically understand which interactions are specific for junction-localized Daple. To this end, Daple was N-terminally tagged with BirA biotin ligase (Figure S4A) and the construct was rigorously validated using several approaches. Immunofluorescence studies confirmed that the exogenously expressed tagged construct localized similarly to the endogenous protein—it is found on cell junctions and the perinuclear recycling compartment (Figures S4B and S4C) as described previously (Aznar et al., 2017). Biotinylation *in situ* was confirmed by incubating cell lysates with streptavidin beads and blotting using fluorescent conjugated streptavidin (Figures 4A and 4B). Immunoblotting and biochemical interaction assays confirmed that the construct was expressed as full-length protein and retained binding to Dvl (Figures S4D and S4E). Staining for biotinylated protein in HEK293T cells revealed that the construct can indeed label proteins at cell junctions (Figure 4B).

MS identification of biotinylated proteins in HEK293T, E-type, and R-type cells revealed several novel binding partners of Daple (Figure 4D). Because Daple's C-terminal PDZ-binding motif (PBM) was deemed

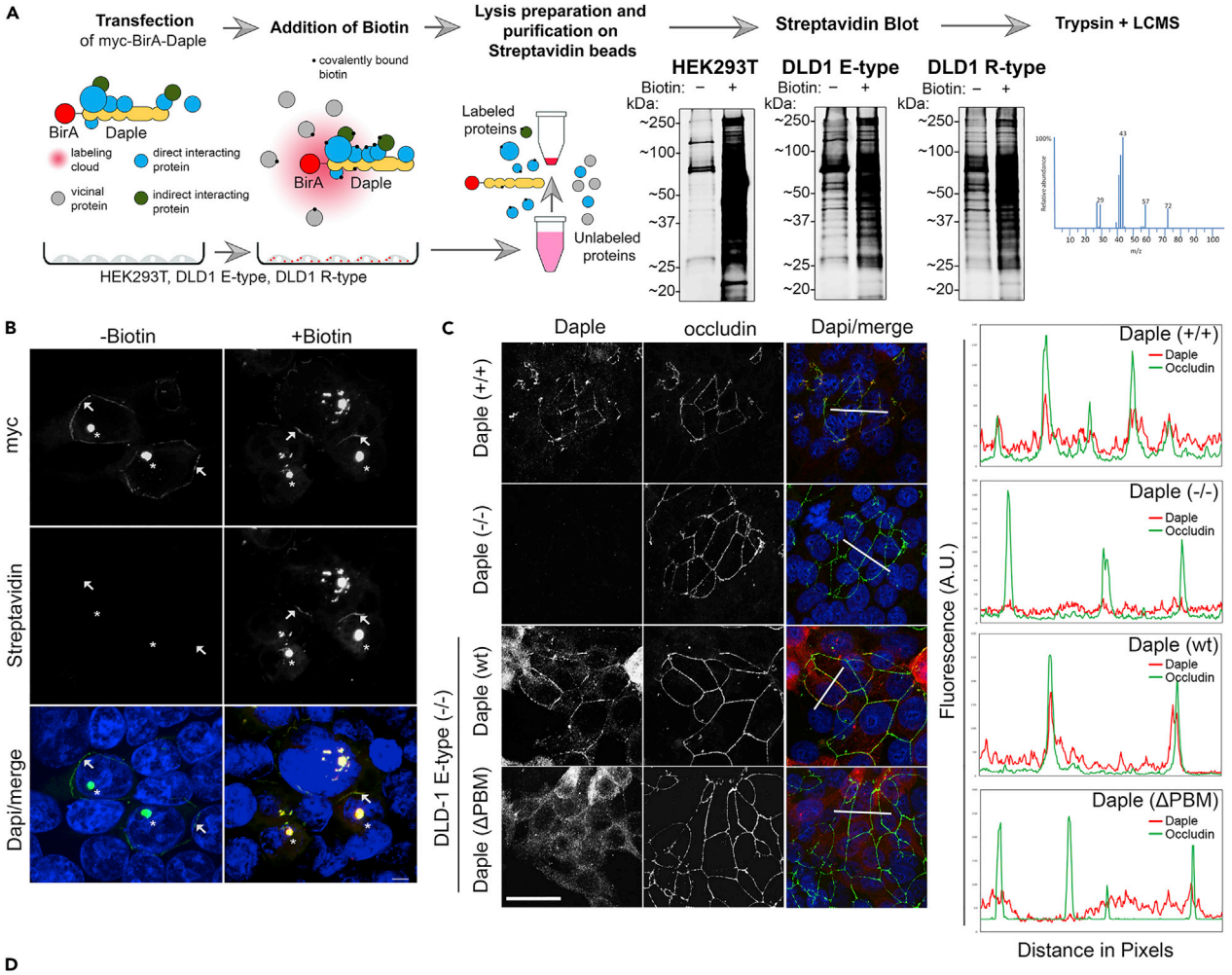
A
Transfection
of myc-BirA-Daple
Addition of Biotin
Lysis preparation and
purification on
Streptavidin beads
Streptavidin Blot
Trypsin + LCMS
• covalently bound
biotin
BirA
Daple
labeling
cloud
direct interacting
protein
vicinal
protein
indirect interacting
protein
HEK293T, DLD1 E-type, DLD1 R-type
Labeled
proteins
Unlabeled
proteins
HEK293T
DLD1 E-type
DLD1 R-type
Biotin: – +
kDa:
~250
~100
~50
~37
~25
~20
B
-Biotin
+Biotin
myc
Streptavidin
Dapi/merge
C
Daple
occludin
Dapi/merge
Daple (+/+)
Daple (-/-)
DLD-1 E-type (-/-)
Daple (wt)
Daple (ΔPBM)
Fluorescence (A.U.)
Daple
Occludin
Distance in Pixels
D
HEK293T
-Biotin
+Biotin
160
234
278
Src homology-3 domain 26
P-loop containing nucleoside triphosphate hydrolase 21
PDZ domain 17
Nucleotide-binding, alpha-beta plait 16
Protein kinase, catalytic domain 16
Protein kinase-like domain 16
Zinc finger, LIM-type 13
Variant SH3 12
RNA recognition motif domain 12
Protein kinase, ATP binding site 12
DLD1 E-type
-Biotin
+Biotin
45
109
142
Intermediate filament protein, conserved site 14
Intermediate filament protein 14
Src homology-3 domain 10
Type II keratin 7
Keratin, type I 7
PDZ domain 7
RNA recognition motif domain 7
Nucleotide-binding, alpha-beta plait 7
Calponin homology domain 6
Zinc finger, LIM-type 5
DLD1 R-type
-Biotin
+Biotin
44
244
296
Nucleotide-binding, alpha-beta plait 24
RNA recognition motif domain 21
Pleckstrin homology-like domain 14
Src homology-3 domain 12
WD40/YVTN repeat-like-containing domain 11
WD40 repeat 10
WD40-repeat-containing domain 10
Serine/threonine-protein kinase, active site 10
Thioredoxin-like fold 8
UBA-like 6

Figure 4. Biotin Proximity Labeling Identifies an Enrichment of PDZ Proteins within Daple's Interactome in E-type, but not in R-type Cells

(A) Schematic summarizing the workflow of biotin proximity labeling study carried out using exogenously expressed myc-BirA-Daple in various cell lines. Immunoblot with Alexa Fluor 680 conjugated streptavidin confirmed biotinylation of affinity purified proteins.

(B) HEK293T cells transfected with myc-BirA-Daple and treated with biotin were stained with Alexa Fluor 594 conjugated streptavidin and antibodies against the myc-tag (*green*). Asterisk, pericentriolar localization; arrow, PM localization. Scale bar, 5 μm.

(C) DLD1 E-type (+/+), E-type (−/−), or Daple (−/−) cells ectopically expressing Daple-WT or Daple-PBM deficient mutants (ΔPBM) were stained for Daple (*red*) and occludin (*green*). *Right*: RGB plot of region indicated in merge panels.

(D) *Top*: Venn Diagram showing overlap of affinity-captured proteins identified by mass spectrometry between biotin-treated or no-biotin-treated control samples. *Bottom*: Bar graph summarizing identified proteins (exclusive to plus biotin conditions) grouped by protein domain using DAVID GO analysis. Top domains categories are shown.

essential for its localization to cell junction (Figure 4C), we carried out gene-ontology (GO) analyses on the MS hits by protein domains (using DAVID GO and INTERPRO domains, with p value < .05 set as significant) expecting to find PDZ-containing proteins that are enriched or eliminated depending on Daple's localization (Figure 4D). Indeed, we found that several PDZ proteins that are associated with cell junctions were enriched in the BioIDs from HEK293T and E-type cells but not in R-type cells (Figures 4D and 5A). It is noteworthy to point out that, although R-type cells did not present a significant enrichment for PDZ proteins, two proteins containing PDZ domains were identified (Figure 5A). These findings led us to hypothesize that Daple may be recruited onto cell junctions by its PBM module via its interaction with PDZ proteins. Henceforth, we directed our efforts at validating *in vitro* some of the putative PDZ-PBM interactions and understanding how those interactions may be reversibly regulated to allow context-dependent localization of Daple at cell junctions.

Daple Directly and Specifically Binds to PDZ Proteins, PARD3, and mPDZ

BioID relies on transient transfection; hence, it is prone to artifacts due to either compromised cell health or higher than physiologic levels of proteins with resultant altered stoichiometry, and only indicates proximity, not direct interaction. We sought to validate our BioID "hits" by asking which PDZ proteins identified by BioID (Figure 5A) directly interact with Daple using recombinant GST-tagged PDZ proteins in *in vitro* interaction assays with purified Daple-CT (aa. 1,650–2,028). Five proteins were prioritized based on the criteria that they are all *bona fide* PDZ family of proteins that localize to cell junctions: (1) the Par-3 Family Cell Polarity Regulator PARD3; (2) the Multiple PDZ Domain Crumbs Cell Polarity Complex Component mPDZ; (3) the tight junction protein 1, TJP1, a.k.a, zonula occludens (ZO)-1, (4) the tight junction protein 2, TJP2, a.k.a, zonula occludens (ZO)-2, and (5) GAIP-interacting protein, C terminus (GIPC) (Funahashi et al., 2013; Meerschaert et al., 2009; Varsano et al., 2012; Baliova et al., 2014). Interaction was detected with PARD3 and mPDZ besides the previously known interacting partner, Dvl. A much weaker interaction was detected between ZO-1 and Daple (Figure 5B). As suspected, all these interactions were virtually lost when we used purified Daple-CT lacking the described C-terminal PBM (ΔPBM) (Figure 5C) or when cell lysates of exogenously expressed full-length Daple (WT or ΔPBM) was used in the interaction assays (Figure 5D). These findings confirm that Daple's interactions with diverse PDZ proteins are likely to be mediated via a PDZ•PBM interaction.

Because both PARD3 and mPDZ are molecular scaffolds that have more than one PDZ domain, we asked if the binding of Daple to these proteins is mediated specifically via one or more of these domains. When we purified each of the 13 PDZ domains of mPDZ from bacteria as GST-tagged proteins and used them in pull-down assays, we found that Daple preferentially bound the third PDZ domain on mPDZ (Figures S5A and S5B). We took a slightly different approach in the case of PARD3, which contains three PDZ domains (Figure 5E). First, we confirmed that binding between Daple and PARD3 is specific to PARD3's PDZ domains (Funahashi et al., 2013), via *in vitro* protein interaction assays with various GST-tagged PARD3 truncation constructs and recombinant His-Daple-CT. Daple specifically binds to the PARD3 construct that contains the PDZ domains (Figure 5E). Next we determined which of the three PDZ domains Daple binds to, by investigating GST-tagged Daple-CT interaction with PARD3 constructs from which individual PDZ domains were deleted (Zhang et al., 2016). Only deletion of the third PDZ (PDZ3) on PARD3 led to loss of binding to Daple (Figure 5F). Taken together with our prior *in vitro* binding studies, we conclude that Daple directly binds to both PARD3 and mPDZ. In each case, the PBM on Daple is required, and the interaction occurs via the ability of the PBM to bind the third PDZ domains of PARD3 or mPDZ. In doing so, Daple's appears to display a high degree of specificity because it binds to only one of 13 PDZ modules on mPDZ and one of three modules in PARD3 (Figures 5F and S5). Thus, the Daple•PBM recognition is specific to a limited set of PDZ proteins and domains.

A

Gene Name	E-type	R-type	HEK293T
Afadin, adherens junction formation factor (AFDN)	✓		
GIPC PDZ domain containing family member 1 (GIPC1)			✓
LIM domain 7 (LMO7)	✓		
Membrane palmitoylated protein 1 (MPP1)			✓
Membrane palmitoylated protein 5 (MPP5)		✓	
Multiple PDZ domain crumbs cell polarity complex component (MPDZ)			✓
Par-3 family cell polarity regulator beta (PARD3B)		✓	✓
Par-3 family cell polarity regulator (PARD3)	✓		
PATJ, crumbs cell polarity complex component (PATJ)	✓		
PDZ and LIM domain 1 (PDLIM1)			✓
PDZ and LIM domain 1 (PDLIM1)	✓		
PDZ and LIM domain 3 (PDLIM3)			✓
PDZ and LIM domain 4 (PDLIM4)			✓
PDZ and LIM domain 5 (PDLIM5)			✓
Protein phosphatase 1 regulatory subunit 9B (PPP1R9B)			✓
Rho GTPase activating protein 21 (ARHGAP21)			✓
Signal induced proliferation associated 1 like 3 (SIPA1L3)			✓
Syndecan binding protein (SDCBP)			✓
Tight junction protein 1 (TJP1) (Zonula Occludens 1, ZO-1)	✓		✓
Tight junction protein 2 (TJP2) (Zonula Occludens 2, ZO-2)	✓		✓

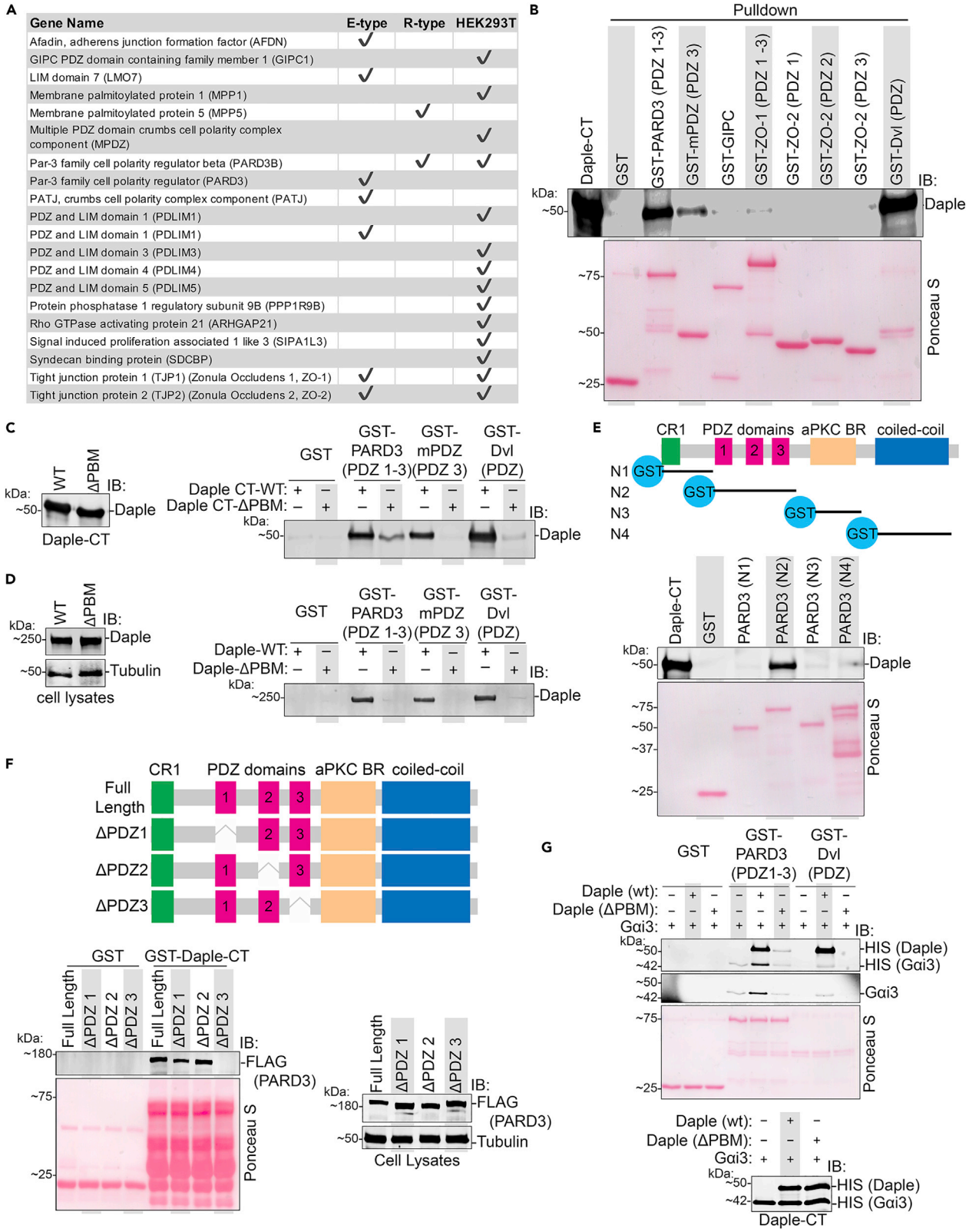

Figure 5. Daple Directly and Selectively Binds to the Third PDZ Module of PARD3 via Its C-terminal PBM and Can Form Ternary Co-complex with Gαi3

(A) Table of PDZ proteins identified by mass spectrometry in BioID studies in Figure 4.

(B) Pull-down assays using purified GST-tagged PDZ domains PARD3, mPDZ, ZO-1, ZO-2, and Dvl immobilized on glutathione beads and soluble recombinant His-Daple-CT. Bound Daple-CT was determined by immunoblotting.

(C) Pull-down assays using GST-tagged PARD3, mPDZ, or Dvl PDZ domains used in binding assays with purified His-Daple-CT-WT or His-Daple-CT-ΔPBM.

(D) Pull-down assays using GST-tagged proteins, as above, where lysates of transiently transfected HEK293T cells were used as source of full-length Daple-WT or Daple-ΔPBM.

(E) *Top*: Schematic shows the modularity of various GST-PARD3 constructs used (N1-N4). *Bottom*: Pull-down assays using various GST-PARD3 regions with Daple-CT. GST-PARD3-bound Daple-CT was analyzed by immunoblotting.

(F) Schematic shows the modularity of various FLAG-PARD3 constructs exogenously expressed in cells and used as source of PARD3 for pull-down assays. *Bottom*: Pull-down assays using various FLAG-tagged PARD3 constructs with recombinant GST-Daple-CT. Daple-CT-bound PARD3 proteins (left) and input lysates for FLAG-PARD3 (right) were analyzed by immunoblotting (left and right, respectively).

(G) Pull-down assays with GST-tagged PARD3 or Dvl PDZ proteins immobilized on glutathione beads and various His-tagged proteins, either alone or in combination, as indicated. Bound complexes and inputs were analyzed by immunoblotting.

Daple, PARD3, and G-Protein Can Form Ternary Complexes

Prior work in *Drosophila* has demonstrated the importance of PARD3 and Gαi in regulating cell polarity and centrosome positioning (Hampoelz et al., 2005; Chia et al., 2008). Because Daple binds and modulates Gαi activity (Aznar et al., 2015), and we now find that it binds PARD3 and regulates PCP, we hypothesized that the Daple•PARD3 interaction may allow scaffolding of G proteins to PARD3 and hence coordinate the establishment of PCP. We began by asking if the newly discovered Daple•PARD3-PDZ interaction affects the Daple•Gαi interaction. We had previously described an unexpected allosteric phenomenon in which the Daple•Dvl-PDZ and the Daple•Gαi interactions are mutually exclusive, i.e., ternary complexes between all three proteins, Gαi•Daple•Dvl is not feasible (Aznar et al., 2018). To our surprise, such allostery was not observed in the case of PARD3; instead, we found that Gαi3 bound PARD3 exclusively in the presence of Daple, and not directly, indicative of the formation of tertiary Gαi•Daple•PARD3 complexes (Figure 5G). This suggests that despite both interactions (Daple•Dvl and Daple•PARD3) occurring via the same Daple's PBM, the exact mechanism of binding may differ between various PDZ domains. Moreover, context-dependent interaction of Daple's PBM with one (Dvl) or the other (PARD3) may impede or enable, respectively, Daple's ability to bind and modulate G-protein signaling.

Tyrosine Phosphorylation of Daple's PBM Shapes Its PDZ-Interactome, Localization to Cell Junctions

The two tyrosines immediately adjacent to Daple's PBM have previously been shown to serve as a platform for convergence of signaling downstream of multiple receptor and non-receptor tyrosine kinases (TKs) like Src (Aznar et al., 2018) (Figure 6A). We asked if these phosphoevents can dictate which PDZ proteins bind Daple. As shown previously, tyrosine phosphorylation of Daple's PBM by Src reduced binding of Daple to Dvl (Aznar et al., 2018); by contrast, phosphorylation enhanced binding to PARD3 under the same conditions (Figures 6B and 6C). We dissected the relative contributions of single phosphorylations at either Y2023 or Y2025 using GST-tagged Daple-PBM (aa. 2,008–2,028) and a previously published strategy of using phosphomimicking mutants (Tyr[Y] to Glu[E]) (Aznar et al., 2018). Mutating either tyrosine residue to glutamate alone did not decrease binding to PARD3; instead, Y2023E enhanced binding to PARD3 (Figures 6D and 6E). By contrast, mutating either Y to E was sufficient to disrupt binding to Dvl (Figures 6D and 6E). The dual phosphomimicking Daple construct bound neither PARD3 nor Dvl. In converse experiments, where GST-PARD3 or GST-Dvl is used to pull down His-Daple-CT, we see similar findings, in that Daple Y2023E alone was sufficient to disrupt the Daple•Dvl interaction (consistent with prior report [Aznar et al., 2018]) but not the Daple•PARD3 interaction (Figures S6A–S6C). Findings from GST-pull-down assays were recapitulated in coimmunoprecipitation studies in cells; immune complexes showed that PARD3 interacts with ectopically expressed Daple-WT or Daple-FA (F1675A, a previously described G-protein binding deficient mutant) but not with Daple-ΔPBM or the dual phosphomimick Daple-Y2023/2025E mutant (Figure 6F). This dual phosphomimic mutant failed to localize to cell junctions (Figure 6G), which is consistent with the defect we observed earlier in the case of the Daple-ΔPBM mutant (Figure 4C). Finally, cells retain the ability to localize PARD3 onto junctions in the absence of Daple (Figure S6D), suggesting that Daple is recruited onto junctions by PDZ domain proteins.

Based on these findings, a picture emerges in which single phosphorylation at Y2023 or Y2025 may be sufficient to disrupt Daple•Dvl, but not Daple•PARD3 interaction, whereas dual site phosphorylation disrupts both. We

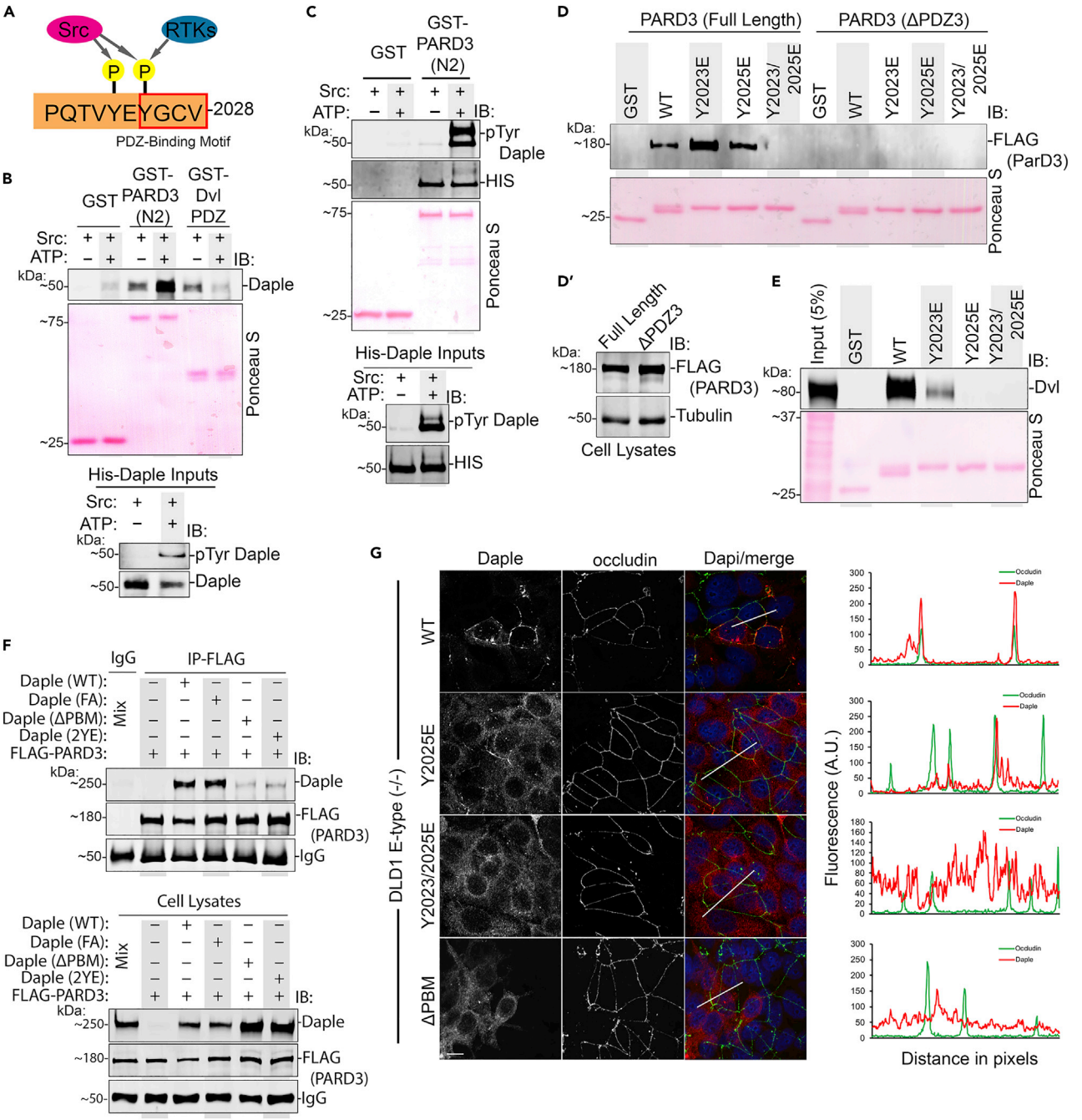

Figure 6. Tyrosine Phosphorylation on Daple's PBM Regulates Its Ability to Bind PARD3

(A) Schematic summarizing published work of Daple's PBM and its tyrosine phosphorylation site by RTKs (i.e., EGFR) or non-RTKs (i.e., Src) (Aznar et al., 2018).

(B and C) Daple-CT phosphorylated *in vitro* by recombinant Src kinase was used in GST-pull-down assays with PARD3-PDZ domains or Dvl-PDZ domain. Bound proteins are analyzed for Daple-CT using total (B) or phospho-specific (C) Daple antibody.

(D and D') GST-tagged phosphomimicking Daple mutants (Y2023E, Y2025E, or double Y2023/2025E) were used in pull-down assays with lysates of transfected HEK293T as source for FLAG-PARD3-full length or PARD3-ΔPDZ3. Bound proteins are analyzed by immunoblotting in (D). Inputs of cell lysates used in pull-down assay were analyzed by immunoblotting in D'.

(E) GST-tagged construct as in (D), used in pull-down assays with lysates of transfected HEK293T as source for Dvl. Bound proteins are analyzed by immunoblotting.

(F) Co-immunoprecipitation assays investigating the binding between FLAG-PARD3 and various Daple mutants (WT, F1675A [FA], ΔPBM, or Y2023/2025E [2YE]). Proteins were exogenously expressed in HEK293T cells followed by cell lysis and IP using anti-FLAG antibody or control IgG.

(G) E-type (−/−) cells transiently expressing Daple-WT, Daple-Y2025E, or Daple-Y2023/2025E stated for Daple (*red*) and occludin (*green*). *Right:* RGB plot of indicated region indicated in merge panels.

A

Daple	PARD3 PDZ3	mPDZ PDZ3	Dvl PDZ	Gαi (GDP)	FZD7
WT	✓	✓	✓	✓	✓
ΔPBM	–	–	–	✓	✓
Y2023E	✓	NT	–	NT	NT
Y2025E	✓	–	–	✓	✓
Y2023E, Y2025E	–	NT	–	✓	✓
Y2023F	✓	NT	–	NT	NT
Y2025F	✓	–	–	NT	NT
Y2023F, Y2025F	✓	NT	–	–	–
E2024A	–	–	–	NT	NT
E2024K	–	–	–	NT	NT

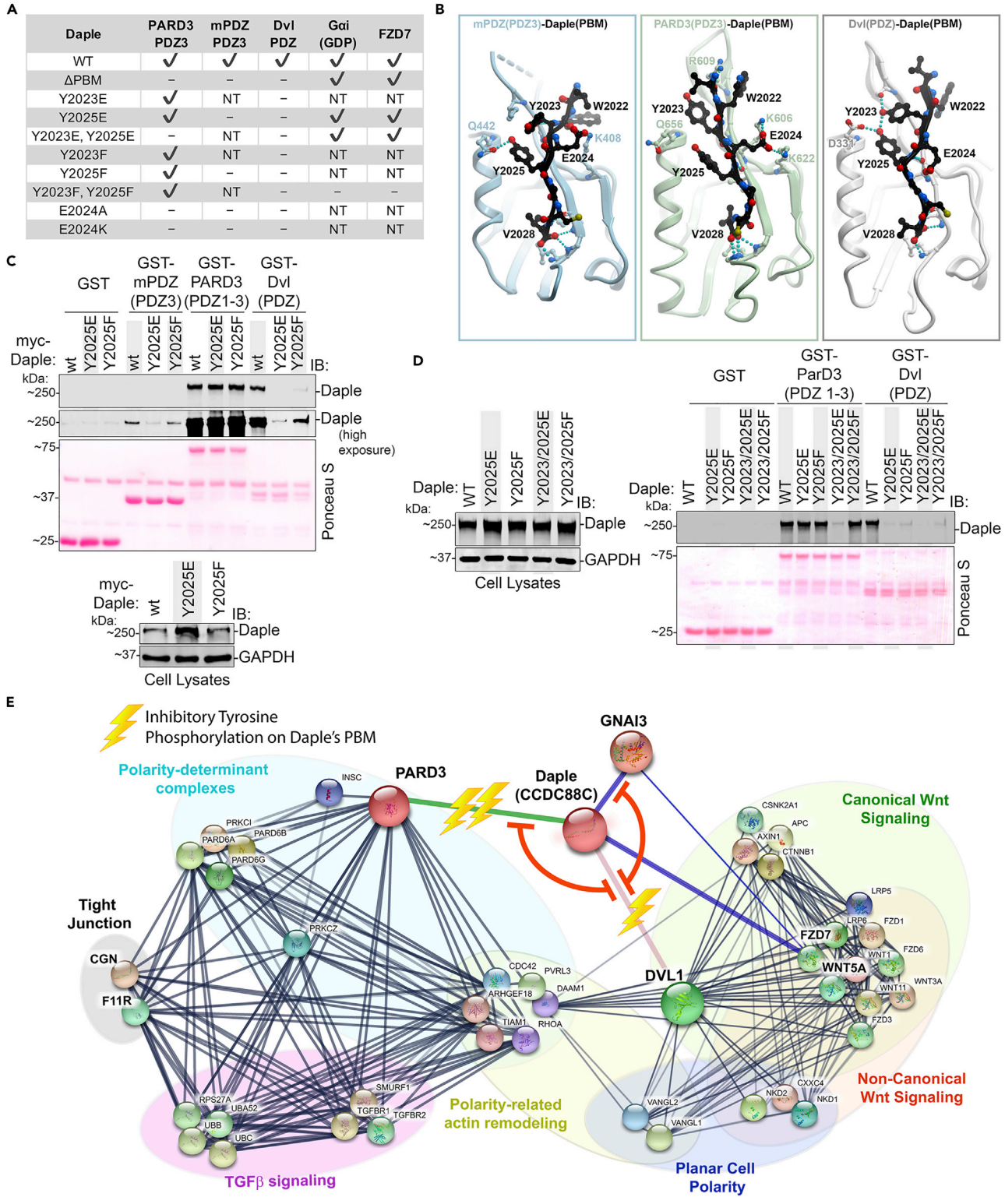

Figure 7. Summary of Findings: Phosphoregulated Assembly of PARD3·Gαi3·Daple, Dvl·Daple and Gαi3·Daple Complexes at Cell-Cell Junctions Fine Tunes Planar Cell Migration

(A) Table summarizing the interactome of Daple's PBM with various PDZ domains and the impact of various mutations tested in this work. NT, not tested.
(B) Homology models of Daple's PBM bound to PDZ domains of PARD3, mPDZ, or Dvl.

Figure 7. *Continued*

(C) Pull-down assay carried out using GST-tagged PDZ domains of mPDZ (PDZ3), PARD3, and Dvl immobilized on glutathione S transferase beads and lysates of transiently transfected HEK293T cells as source for WT and mutants of myc-Daple (Daple-WT, phosphomimicking Daple-Y2025E, or unphosphorylated Daple-Y2025F). Immunoblots show bound proteins and confirm expression of Daple in cell lysates (input).

(D) GST pull-down assay carried out using GST-tagged PDZ domains of PARD3 and Dvl and lysates of transiently transfected HEK293T cells as source for WT and mutants of myc-Daple. Bound proteins were visualized by immunoblotting.

(E) A protein-protein interaction network built using STRING (Snel et al., 2000; Szklarczyk et al., 2019) depicts how Daple may regulate various closely related biological processes via its interactions with PARD3, Dvl, and Gαi. Mutual exclusivity between complexes (red lines) and the impact of tyrosine phosphorylation in each interaction (bolt, inhibitory effect) is shown.

previously showed that neither phosphoevent, alone or in combination, impacts Daple's ability to bind Gαi or FDZ (Aznar et al., 2018) (Figure 7A). We conclude that graded phosphorylation of Daple's PBM may regulate the composition of Daple-bound complexes and may contribute, in part, to the dynamic spatial temporal control over their assembly/disassembly by tyrosine-based signals. To confirm if these events regulate planar migration, we generated "rescue" cell lines in which Daple-WT or two specific mutants that cannot bind PARD3 were stably expressed in Daple-depleted DLD1 cells. We noted that the levels of expression of Daple constructs were well above endogenous levels (Figure S6E) and that the constructs were expressed heterogeneously (Figure S6F). When we set out to carry out the polarized radial migration assays from the edge of tumor spheroids, we noted that all "rescue" cell lines failed to form true compact spheroids like the parental line (Figure S6G). Because compact spheroids are a pre-requisite to study planar migration in the setting of intact junctions (Kramer et al., 2013), and because of the importance of physiologic stoichiometry of signaling and scaffolding proteins (Wu et al., 2011; Bernick et al., 2010; Wang et al., 2014), we did not proceed with radial migration assays in these lines. Future studies with sophisticated methods will be needed, e.g., genetic knockin of the specific mutations so that endogenous levels can be achieved through its natural promoter. Given these limitations observed in cell lines, and in light of recently published *in vivo* findings using *Xenopus laevis* (Marivin and Garcia-Marcos, 2019), we conclude that the impact of phosphoevents we observe here on Daple-bound complexes *in vitro* may contribute to dynamic regulation of Daple-dependent signaling at cell-cell junctions in the epithelium.

Homology Modeling Reveals Subtle Differences between Various Daple-PBM•PDZ Complexes

To rationalize why some Daple-PBM•PDZ interactions were more sensitive to tyrosine phosphorylations (Dvl and mPDZ) than others (PARD3), we carried out 3D homology modeling using a previously solved structure of the PDZ domains of PARD3, Dvl, and mPDZ, in complex with peptide ligands. Both Y2023 and Y2025 form hydrogen bonds (H-bonds) with Dvl, which explains why the removal of the hydroxyl group (through phosphorylation, Y > E, or Y > F mutation) on either tyrosine abolishes Daple interaction with Dvl (Figure 7B). Only Y2025 on Daple forms an H-bond with mPDZ (to Q442), explaining similar detrimental effects of Y2025E and Y2025F on mPDZ binding to Daple. Similar to what was observed on Dvl, the Y2025E mutant showed a greater decrease in binding compared with Y2025F (Figure 7C). Homology modeling studies suggested that neither of the tyrosine residues contributes substantially to Daple's interaction with the third PDZ domain of PARD3. This explains why mutation of either Y2023 or Y2025 to E or to F does not cause a loss of binding between Daple and PARD3 (Figure 7D). The increase in binding between PARD3 and Daple-Y2023E mutant and phosphorylated Daple can be explained by the increase in charge interaction between Y2023 and R609 on PARD3 (Figures 6B–6D and 7B).

The models also shed additional insights into the subtle differences in Daple's ability to bind diverse PDZ domains: instead of the tyrosines, the key determinant of Daple binding to PARD3 and mPDZ is E2024, which forms a salt bridge with K606 and K622 (PARD3) and with K408 (mPDZ). Because Dvl lacks basic residues in the corresponding positions, the salt bridge is absent in the Daple•Dvl complex; however, E2024 appears to engage with the backbone of I282 (Dvl) via H-bonding. In keeping with these modeling-based predictions, GST-Daple-PBM with an E2024 mutation to Alanine (A) or Lysine (K) also abolished binding to PARD3 and Dvl (Figures S7A and S7B). In the reciprocal assays, when GST-PDZ protein was used to pull down full length Daple form cell lysates, Daple-E2024A and E2024K mutants showed decreased binding to all three PDZ proteins, albeit to variable degrees (Figure S7C). The varying degrees of Daple•PARD3 or Daple•Dvl interactions observed in pull-down assays interchangeably using one binding partner as bacterially expressed GST protein and another from cell lysates suggest that the interaction in cells may be more complex (i.e., subjected to additional posttranslational modifications) than what can be reconstituted in *in vitro* studies.

Together, our findings indicate that, despite the overall shared modality of binding between Daple and the three PDZ proteins, subtle differences exist between the Daple-PBM•PDZ interface assembled in each case. These differences could account for their differential sensitivity to disruption by tyrosine phosphorylations at the two sites on Daple's PBM. Furthermore, a STRING (Snel et al., 2000; Szklarczyk et al., 2019) protein-protein interaction network shows that the disruptive phosphoevents on Daple's PBM could provide a molecular basis for how tyrosine-based signals can initiate or terminate conditional and contextual scaffolding of key proteins within discrete pathways and cellular processes (Figure 7E).

DISCUSSION

The major discovery we report here is that junction-localized Daple scaffolds PDZ-containing polarity regulator PARD3 to maintain contact-triggered polarization during migration in 2D planes. We also demonstrate how growth factors may shape these scaffolding functions of Daple via their ability to trigger two key tyrosine phosphoevents targeting Daple's PBM. These phosphoevents dictate the localization of Daple, as well as its interactome: Daple that is not phosphorylated or hypophosphorylated (i.e., only on one tyrosine) may bind PARD3 and localize to the junctions; however, Daple that is hyperphosphorylated (i.e., on both tyrosines) may not bind either; instead, it localizes to the cytoplasm and may continue to modulate G protein signaling downstream of Wnt/FZD. Overall, our findings show that unphosphorylated Daple has maximal localization at cell-cell junctions; dually phosphorylated Daple (by Src family of kinases) cannot localize to junctions; the mono-phosphorylated Daple has an intermediate hypomorphic characteristic.

These mechanistic studies, in conjunction with our prior work elucidating the effects of growth factor RTKs and growth factor stimulated non-RTKs on Daple (Aznar et al., 2018), support the following working model in which the Daple•PARD3 interaction may serve as a critical determinant of localization of Daple at cell junctions. Once at junctions, Daple may orchestrate what appears to be a graded response to varying concentrations of growth factors: When growth factor concentrations are low (presumably triggering low-grade RTK activation), hypophosphorylated Daple bound to PARD3 promotes contact-triggered polarization during migration; however, when growth factors are high, hyperphosphorylated Daple dissociates from PARD3 and potentiates contact-free cell scattering.

Our findings also shed light into the two seemingly opposite ways in which Daple influences cancer initiation and progression; it acts as tumor suppressor in the normal epithelium and during early stages while supporting EMT/invasion during late stages (Aznar et al., 2015; Dunkel et al., 2018). This bifaceted role is shared by two other prominent signaling pathways—TGF-β and the non-canonical β-catenin-independent signaling that is triggered by Wnt5A/FZD7 (Akhurst and Derynck, 2001; McDonald and Silver, 2009). By scaffolding both these pathways to cell junctions (see Figure 7E), Daple may enable these growth factor signals to support seemingly opposite responses in cells with or without stable junctions. Cells with junctions, such as normal epithelium or in early-staged well-differentiated tumors, elicit contact-triggered orientation and contact-dependent planar migration. By contrast, cells without junctions, such as poorly differentiated tumors, elicit contact-free migration/EMT. Thus, it is possible that the seemingly opposing roles of Daple may be due to the presence or absence of cell-cell junctions and Daple's localization to those junctions.

As for the relevance of our findings during development, it is noteworthy that mutations in Daple (that eliminate its PBM) have been identified in patients with non-syndromic hydrocephalus and depletion of Daple in animal models lead to hydrocephalus as well as ear/hearing defects (Drielsma et al., 2012; Siletti et al., 2017; Takagishi et al., 2017; Marivin and Garcia-Marcos, 2019; Marivin et al., 2019). Underlying both conditions is a failure to polarize the cells and position the cilia. Our work provides mechanistic insights into how Daple may maintain contact-triggered cellular orientation in polarized cells with intact junctions. It is possible that the mechanisms we delineate here in colon epithelial cells are fundamental and hold true in other instances.

Limitations of the Study

There may be other PDZ domain proteins that bind to Daple's PBM that was not identified in our screens because of the context of our experimental design (i.e., steady-state culture conditions). Performing similar proteomic studies under various context such as ligand stimulation or using various cell types may expand the repertoire of PDZ interactome to Daple.

Overexpression studies are prone to artifacts owing to mislocalization of proteins and saturation of key binding partners. Genetic knockins of specific mutants may overcome such limitations with overexpression systems and may help in further elucidating the specific functions of key tyrosine residues on Daple's PBM.

METHODS

All methods can be found in the accompanying Transparent Methods supplemental file.

DATA AND CODE AVAILABILITY

We have not generated software, and raw data of MS hits are available upon request from authors.

SUPPLEMENTAL INFORMATION

Supplemental Information can be found online at https://doi.org/10.1016/j.isci.2020.100859.

ACKNOWLEDGMENTS

This paper was supported by NIH, United States, CA238042, CA100768, and CA160911 (to P.G.). J.E was supported by an NCI/NIH-funded Cancer Biology, Informatics & Omics (CBIO) Training Program (T32 CA067754), United States, and a Postdoctoral Fellowship from the American Cancer Society, United States, (PF-18-101-01- CSM). I.K. was supported by NIH, United States, grants GM071872, AI118985, and GM117424. We thank Lee Swanson, Ying Dunkel, Nina Sun, and Camille Delbrook for technical support in this work. We also thank Dr. Soumita Das at the UC San Diego HUMANOID CoRE for access to human organoids.

AUTHOR CONTRIBUTIONS

J.E., A.S., N.R., J.C., and P.G. designed, performed, and analyzed most of the experiments in this work. I.K. generated the homology model for Daple-bound PARD3, mPDZ, and Dvl and provided structure-based guidance to study Daple. M.G. performed the mass spectrometry analysis. J.E. and P.G. conceived the project and wrote the manuscript.

DECLARATION OF INTERESTS

The authors declare no competing interests.

Received: August 9, 2019
Revised: November 27, 2019
Accepted: January 16, 2020
Published: February 21, 2020

REFERENCES

Akhurst, R.J., and Derynck, R. (2001). TGF-beta signaling in cancer–a double-edged sword. Trends Cell Biol. *11*, S44–S51.

Aznar, N., Ear, J., Dunkel, Y., Sun, N., Satterfield, K., He, F., Kalogriopoulos, N.A., Lopez-Sanchez, I., Ghassemian, M., Sahoo, D., et al. (2018). Convergence of Wnt, growth factor, and heterotrimeric G protein signals on the guanine nucleotide exchange factor Daple. Sci. Signal. *11*, https://doi.org/10.1126/scisignal.aao4220.

Aznar, N., Midde, K.K., Dunkel, Y., Lopez-Sanchez, I., Pavlova, Y., Marivin, A., Barbazan, J., Murray, F., Nitsche, U., Janssen, K.P., et al. (2015). Daple is a novel non-receptor GEF required for trimeric G protein activation in Wnt signaling. Elife *4*, e07091.

Aznar, N., Sun, N., Dunkel, Y., Ear, J., Buschman, M.D., and Ghosh, P. (2017). A Daple-Akt feed-forward loop enhances noncanonical Wnt signals by compartmentalizing beta-catenin. Mol. Biol. Cell *28*, 3709–3723.

Baliova, M., Juhasova, A., and Jursky, F. (2014). Using a collection of MUPP1 domains to investigate the similarities of neurotransmitter transporters C-terminal PDZ motifs. Biochem. Biophys. Res. Commun. *454*, 25–29.

Bernick, E.P., Zhang, P.J., and Du, S. (2010). Knockdown and overexpression of Unc-45b result in defective myofibril organization in skeletal muscles of zebrafish embryos. BMC Cell Biol. *11*, 70.

Bhat, A.A., Uppada, S., Achkar, I.W., Hashem, S., Yadav, S.K., Shanmugakonar, M., Al-Naemi, H.A., Haris, M., and Uddin, S. (2018). Tight junction proteins and signaling pathways in cancer and inflammation: a functional crosstalk. Front. Physiol. *9*, 1942.

Chia, W., Somers, W.G., and Wang, H. (2008). Drosophila neuroblast asymmetric divisions: cell cycle regulators, asymmetric protein localization, and tumorigenesis. J. Cell Biol. *180*, 267–272.

Ciasca, G., Papi, M., Minelli, E., Palmieri, V., and De Spirito, M. (2016). Changes in cellular mechanical properties during onset or progression of colorectal cancer. World J. Gastroenterol. *22*, 7203–7214.

Dohn, M.R., Mundell, N.A., Sawyer, L.M., Dunlap, J.A., and Jessen, J.R. (2013). Planar cell polarity proteins differentially regulate extracellular matrix organization and assembly during zebrafish gastrulation. Dev. Biol. *383*, 39–51.

Drielsma, A., Jalas, C., Simonis, N., Desir, J., Simanovsky, N., Pirson, I., Elpeleg, O., Abramowicz, M., and Edvardson, S. (2012). Two novel CCDC88C mutations confirm the role of DAPLE in autosomal recessive congenital hydrocephalus. J. Med. Genet. *49*, 708–712.

Dunkel, Y., Reid, A.L., Ear, J., Aznar, N., Millward, M., Gray, E., Pearce, R., Ziman, M., and Ghosh, P. (2018). Prognostic relevance of CCDC88C (Daple) transcripts in the peripheral blood of patients with cutaneous melanoma. Sci. Rep. *8*, 18036.

Farquhar, M.G., and Palade, G.E. (1963). Junctional complexes in various epithelia. J. Cell Biol. *17*, 375–412.

Fatehullah, A., Appleton, P.L., and Nathke, I.S. (2013). Cell and tissue polarity in the intestinal tract during tumourigenesis: cells still know the right way up, but tissue organization is lost. Philos. Trans. R. Soc. Lond. B Biol. Sci. *368*, 20130014.

Feigin, M.E., and Muthuswamy, S.K. (2009). Polarity proteins regulate mammalian cell-cell junctions and cancer pathogenesis. Curr. Opin. Cell Biol. *21*, 694–700.

Funahashi, Y., Namba, T., Fujisue, S., Itoh, N., Nakamuta, S., Kato, K., Shimada, A., Xu, C., Shan, W., Nishioka, T., and Kaibuchi, K. (2013). ERK2-mediated phosphorylation of Par3 regulates neuronal polarization. J. Neurosci. *33*, 13270–13285.

Gandalovicova, A., Vomastek, T., Rosel, D., and Brabek, J. (2016). Cell polarity signaling in the plasticity of cancer cell invasiveness. Oncotarget *7*, 25022–25049.

Hampoelz, B., Hoeller, O., Bowman, S.K., Dunican, D., and Knoblich, J.A. (2005). Drosophila Ric-8 is essential for plasma-membrane localization of heterotrimeric G proteins. Nat. Cell Biol. *7*, 1099–1105.

Henderson, D.J., Long, D.A., and Dean, C.H. (2018). Planar cell polarity in organ formation. Curr. Opin. Cell Biol. *55*, 96–103.

Ishida-Takagishi, M., Enomoto, A., Asai, N., Ushida, K., Watanabe, T., Hashimoto, T., Kato, T., Weng, L., Matsumoto, S., Asai, M., et al. (2012). The Dishevelled-associating protein Daple controls the non-canonical Wnt/Rac pathway and cell motility. Nat. Commun. *3*, 859.

Knights, A.J., Funnell, A.P., Crossley, M., and Pearson, R.C. (2012). Holding tight: cell junctions and cancer spread. Trends Cancer Res. *8*, 61–69.

Kobayashi, H., Michiue, T., Yukita, A., Danno, H., Sakurai, K., Fukui, A., Kikuchi, A., and Asashima, M. (2005). Novel Daple-like protein positively regulates both the Wnt/beta-catenin pathway and the Wnt/JNK pathway in Xenopus. Mech. Dev. *122*, 1138–1153.

Kramer, N., Walzl, A., Unger, C., Rosner, M., Krupitza, G., Hengstschlager, M., and Dolznig, H. (2013). In vitro cell migration and invasion assays. Mutat. Res. *752*, 10–24.

Marivin, A., and Garcia-Marcos, M. (2019). DAPLE and MPDZ bind to each other and cooperate to promote apical cell constriction. Mol. Biol. Cell *30*, 1900–1910.

Marivin, A., Morozova, V., Walawalkar, I., Leyme, A., Kretov, D.A., Cifuentes, D., Dominguez, I., and Garcia-Marcos, M. (2019). GPCR-independent activation of G proteins promotes apical cell constriction in vivo. J. Cell Biol. *218*, 1743–1763.

Martin, T.A., Mason, M.D., and Jiang, W.G. (2011). Tight junctions in cancer metastasis. Front. Biosci. (Landmark Ed.) *16*, 898–936.

McDonald, S.L., and Silver, A. (2009). The opposing roles of Wnt-5a in cancer. Br. J. Cancer *101*, 209–214.

Meerschaert, K., Tun, M.P., Remue, E., De Ganck, A., Boucherie, C., Vanloo, B., Degeest, G., Vandekerckhove, J., Zimmermann, P., Bhardwaj, N., et al. (2009). The PDZ2 domain of zonula occludens-1 and -2 is a phosphoinositide binding domain. Cell Mol Life Sci *66*, 3951–3966.

Nakamura, N., Lowe, M., Levine, T.P., Rabouille, C., and Warren, G. (1997). The vesicle docking protein p115 binds GM130, a cis-Golgi matrix protein, in a mitotically regulated manner. Cell *89*, 445–455.

Nakamura, N., Rabouille, C., Watson, R., Nilsson, T., Hui, N., Slusarewicz, P., Kreis, T.E., and Warren, G. (1995). Characterization of a cis-Golgi matrix protein, GM130. J. Cell Biol. *131*, 1715–1726.

Rodriguez-Boulan, E., and Macara, I.G. (2014). Organization and execution of the epithelial polarity programme. Nat. Rev. Mol. Cell Biol *15*, 225–242.

Schmoranzer, J., Fawcett, J.P., Segura, M., Tan, S., Vallee, R.B., Pawson, T., and Gundersen, G.G. (2009). Par3 and dynein associate to regulate local microtubule dynamics and centrosome orientation during migration. Curr. Biol. *19*, 1065–1074.

Schneeberger, K., Roth, S., Nieuwenhuis, E.E.S., and Middendorp, S. (2018). Intestinal epithelial cell polarity defects in disease: lessons from microvillus inclusion disease. Dis. Model. Mech. *11*, https://doi.org/10.1242/dmm.031088.

Siletti, K., Tarchini, B., and Hudspeth, A.J. (2017). Daple coordinates organ-wide and cell-intrinsic polarity to pattern inner-ear hair bundles. Proc. Natl. Acad. Sci. U S A *114*, E11170–E11179.

Snel, B., Lehmann, G., Bork, P., and Huynen, M.A. (2000). STRING: a web-server to retrieve and display the repeatedly occurring neighbourhood of a gene. Nucleic Acids Res. *28*, 3442–3444.

Subbaiah, V.K., Kranjec, C., Thomas, M., and Banks, L. (2011). PDZ domains: the building blocks regulating tumorigenesis. Biochem. J. *439*, 195–205.

Szklarczyk, D., Gable, A.L., Lyon, D., Junge, A., Wyder, S., Huerta-Cepas, J., Simonovic, M., Doncheva, N.T., Morris, J.H., Bork, P., et al. (2019). STRING v11: protein-protein association networks with increased coverage, supporting functional discovery in genome-wide experimental datasets. Nucleic Acids Res. *47*, D607–D613.

Takagishi, M., Sawada, M., Ohata, S., Asai, N., Enomoto, A., Takahashi, K., Weng, L., Ushida, K., Ara, H., Matsui, S., et al. (2017). Daple coordinates planar polarized microtubule dynamics in ependymal cells and contributes to hydrocephalus. Cell Rep. *20*, 960–972.

van Hengel, J., Gohon, L., Bruyneel, E., Vermeulen, S., Cornelissen, M., Mareel, M., and von Roy, F. (1997). Protein kinase C activation upregulates intercellular adhesion of alpha-catenin-negative human colon cancer cell variants via induction of desmosomes. J. Cell Biol. *137*, 1103–1116.

Varsano, T., Taupin, V., Guo, L., Baterina, O.Y., Jr., and Farquhar, M.G. (2012). The PDZ protein GIPC regulates trafficking of the LPA1 receptor from APPL signaling endosomes and attenuates the cell's response to LPA. PLoS One *7*, e49227.

Vermeulen, S.J., Bruyneel, E.A., Bracke, M.E., De Bruyne, G.K., Vennekens, K.M., Vleminckx, K.L., Berx, G.J., van Roy, F.M., and Mareel, M.M. (1995). Transition from the noninvasive to the invasive phenotype and loss of alpha-catenin in human colon cancer cells. Cancer Res. *55*, 4722–4728.

Wang, P., Zhou, Z., Hu, A., Ponte de Albuquerque, C., Zhou, Y., Hong, L., Sierecki, E., Ajiro, M., Kruhlak, M., Harris, C., et al. (2014). Both decreased and increased SRPK1 levels promote cancer by interfering with PHLPP-mediated dephosphorylation of Akt. Mol. Cell *54*, 378–391.

Wu, C.Y., Jhingory, S., and Taneyhill, L.A. (2011). The tight junction scaffolding protein cingulin regulates neural crest cell migration. Dev. Dyn. *240*, 2309–2323.

Yi, W., Xiao, E., Ding, R., Luo, P., and Yang, Y. (2016). High expression of fibronectin is associated with poor prognosis, cell proliferation and malignancy via the NF-kappaB/p53-apoptosis signaling pathway in colorectal cancer. Oncol. Rep. *36*, 3145–3153.

Zhang, P., Wang, S., Wang, S., Qiao, J., Zhang, L., Zhang, Z., and Chen, Z. (2016). Dual function of partitioning-defective 3 in the regulation of YAP phosphorylation and activation. Cell Discov. *2*, 16021.

iScience, Volume *23*

Supplemental Information

Tyrosine-Based Signals Regulate the Assembly of Daple·PARD3 Complex at Cell-Cell Junctions

Jason Ear, Anokhi Saklecha, Navin Rajapakse, Julie Choi, Majid Ghassemian, Irina Kufareva, and Pradipta Ghosh

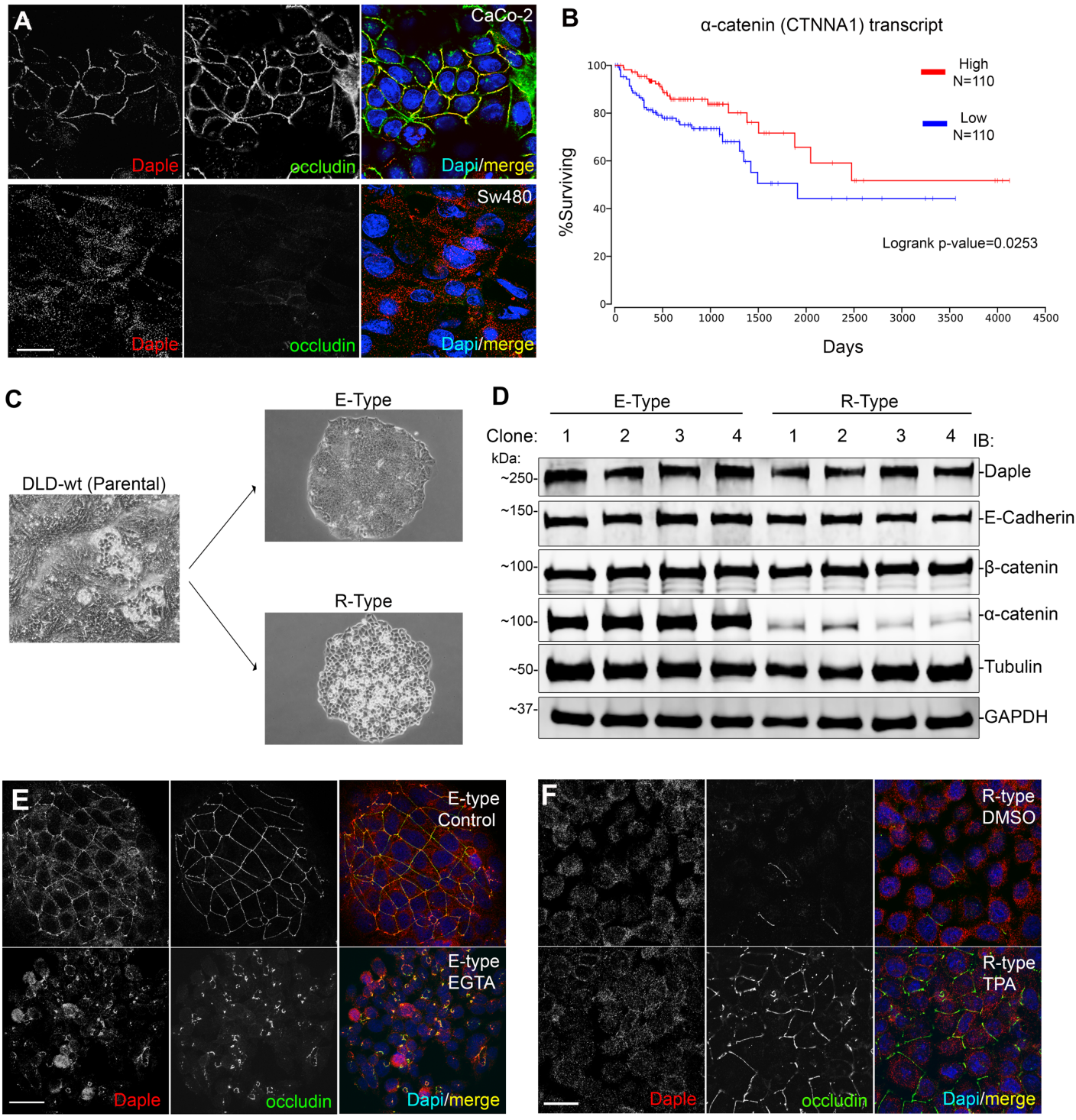

Figure S1-Related to Figure 2. Daple localization and expression in colorectal cancer cell lines.

Figure S1-Related to Figure 2. Daple localization and expression in colorectal cancer cell lines.

A) CaCo-2 (*top*) and Sw480 (*bottom*) colorectal cancer cells were fixed with methanol, stained for Daple (*red*), occludin (*green*) and nucleus (DAPI; blue) and analyzed by confocal microscopy. Representative images are shown. Scale Bar, 25μm. **B)** A Kaplan Meier Plot was generated using OncoLnc (www.oncolnc.org) to compare the disease-free survival rates of patients with colorectal tumors with high vs. low levels of α-catenin expression. OncoLnc links The Cancer Genome Atlas (TCGA; NCI) survival data to mRNA levels (Anaya, 2016). High and low expression is defined as patients with top 25% and bottom 25% expression level, respectively. **C)** Parental DLD1 cells were diluted onto tissue culture plates to produce isolated colonies and imaged by light microscopy. Representative images of those colonies are shown. **D)** Whole cell lysates from clonally isolated colonies were analyzed for expression of Daple, E-cadherin, β-catenin, α-catenin, tubulin and GAPDH by immunoblotting (IB). **E)** EGTA (30 mins) was used to deplete calcium levels and disrupt cell junctions in DLD1 E-type cells. After treatment, cells were fixed and stained for Daple (*red*) and occludin (*green*) and assessed by confocal microscopy. Representative images are shown. Scale Bar, 25μm **F)** TPA (3 hours) was used to activate PKC and transiently restore junctions in R-type cells. Post treatment, cells were fixed and stained for Daple (*red*) and occludin (*green*). Although junctions were restored (as determined by occludin staining), Daple was not recruited to cell-cell junctions. Scale Bar, 25μm.

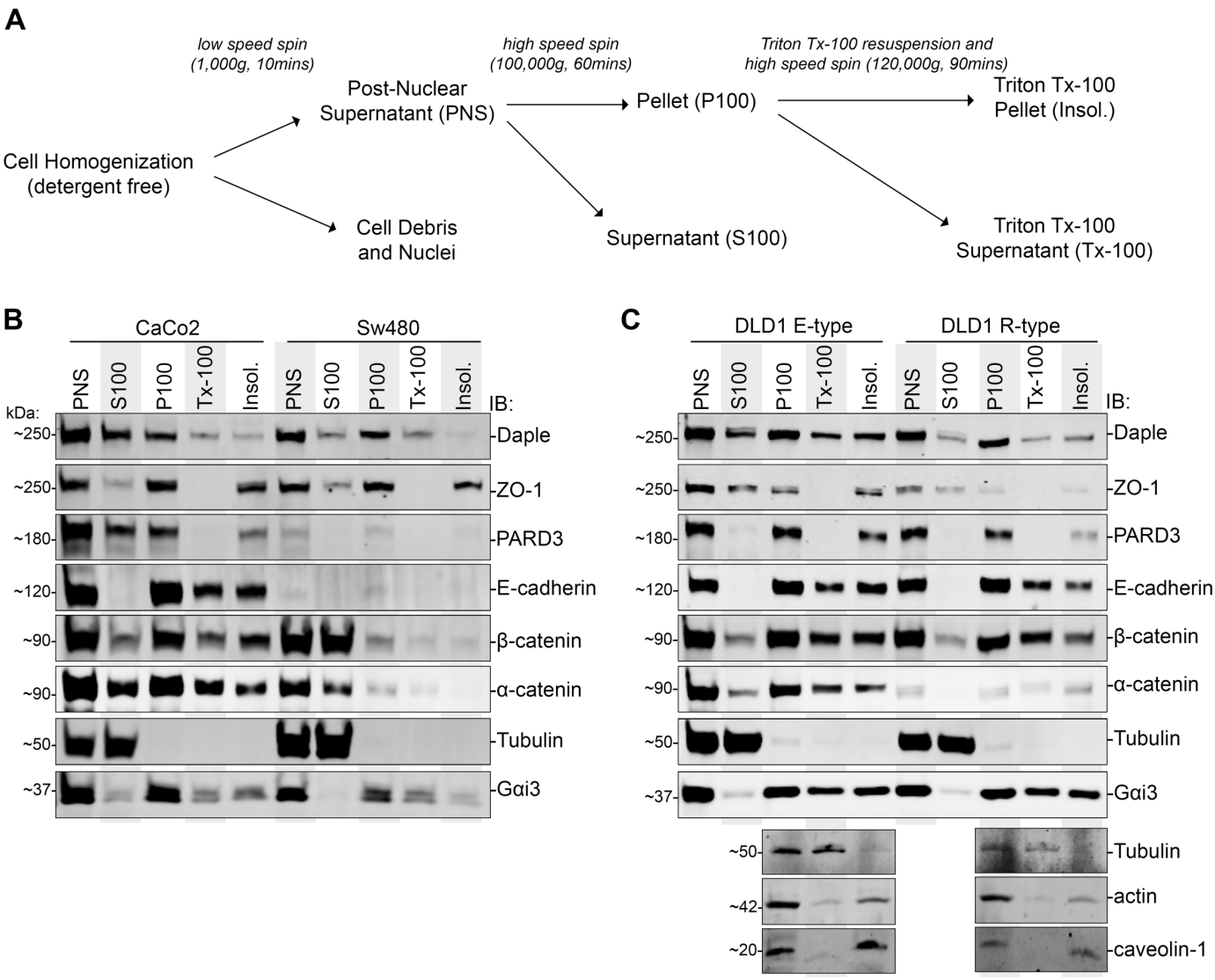

Figure S2-Related to Figure 2. Subcellular fractionation studies on colorectal cancer cells reveal a pool of Daple that is on membrane and is detergent insoluble.

Figure S2-Related to Figure 2. Subcellular fractionation studies on colorectal cancer cells reveal a pool of Daple that is on membrane and is detergent insoluble.

A) Schematic and workflow for subcellular fractionation used in panels B (CaCo-2 and Sw480 cells) and C (DLD1 E-type and R-type cells). Nuclear free cell homogenates (PNS, post nuclear supernatant) in detergent free buffer was spun at 100,000 g to isolate cell membrane (P100, pellet 100,000 g) from cytosol (S100, supernatant 100,000 g). P100 fraction was then resuspended in buffer containing detergent, Triton Tx-100, and centrifuged at 120,000 g to isolate detergent soluble (Tx-100) from detergent insoluble (Insol.) fractions. **B-C)** Daple expression was determined in various cellular fractions by immunoblotting (IB). As controls, Gαi3 and E-cadherin was used to confirm membrane enrichment, whereas tubulin was used to determine cytosol enrichment. Membrane associated ZO-1 and PARD3 was observed in Tx-100 insoluble fractions whereas E-cadherin, β-catenin, and α-catenin was observed in both Tx-100 soluble and insoluble fractions. **C)** Lower panels show higher loading volume of P100, Tx-100, and Insoluble fractions of DLD1 E-type and R-type cells. Actin and Tubulin was used to confirm presence of cytoskeletal proteins. Caveolin-1 was used to confirm presence of lipid rafts.

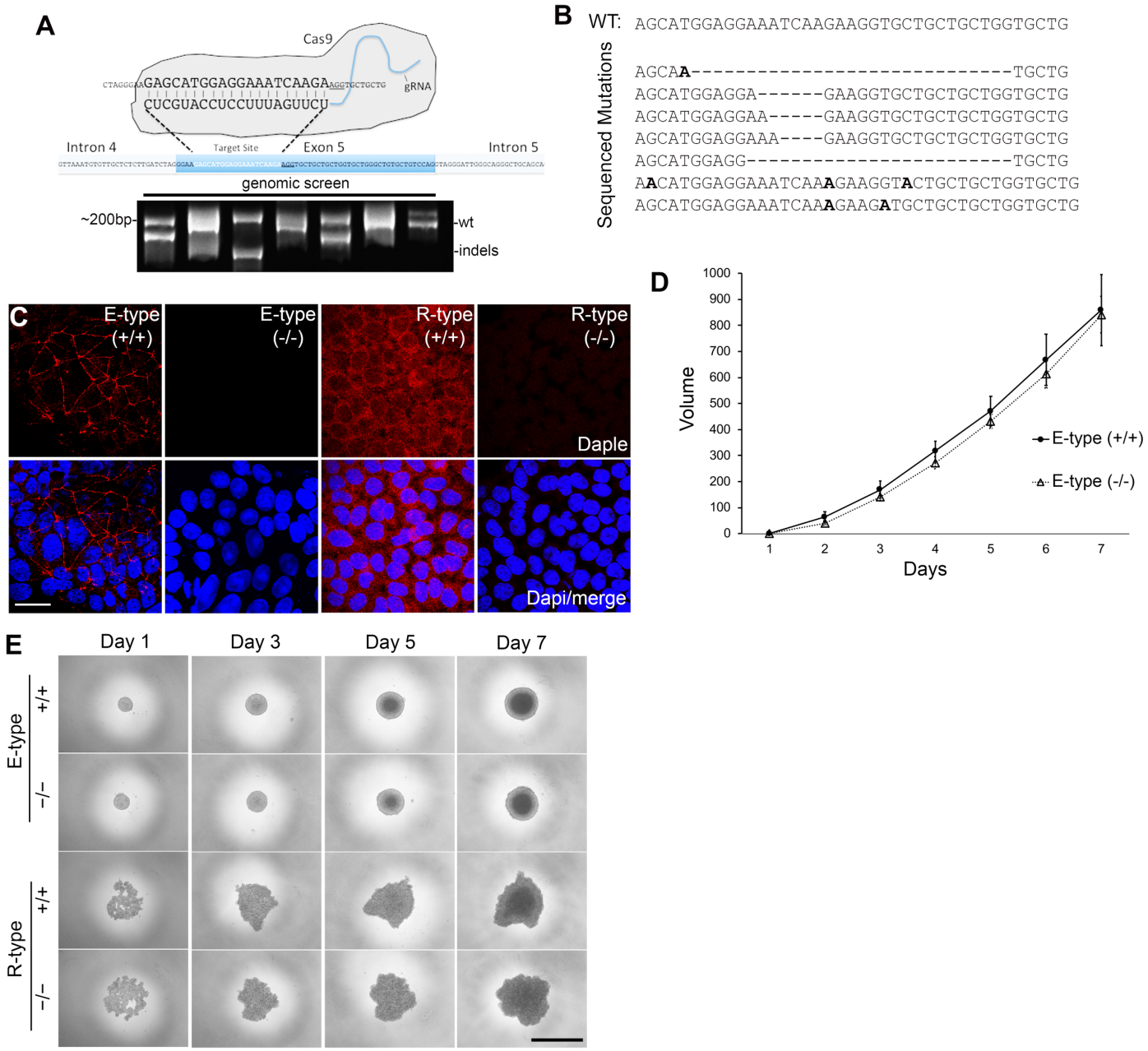

Figure S3-Related to Figure 2. Characterization and validation of Daple CRISPR/Cas9 knockout

Figure S3-Related to Figure 2. Characterization and validation of Daple CRISPR/Cas9 knockout

A) Schematic illustrating Cas9 target site on Exon 5 of Daple (*top*). PCR of region flanking target site using genomic DNA from various cell clones from Cas9 selection (*bottom*). **B)** Representative mutations identified through TOPO-TA cloning and sequencing of amplicons in (A). **C)** DLD1 E-type and R-type cell clones were fixed and stained for Daple (*red*). Scale bar, 25μm. **D)** Graph showing the volume of DLD1 E-type (+/+ and -/-) spheroids in panel E over time, as determined by ImageJ. **E)** Daple depleted DLD1 E-type and R-type cells were grown in agarose-coated plates for 7 days and serially imaged by light microscopy. Representative images of spheroids are shown. Scale bar, 1mm.

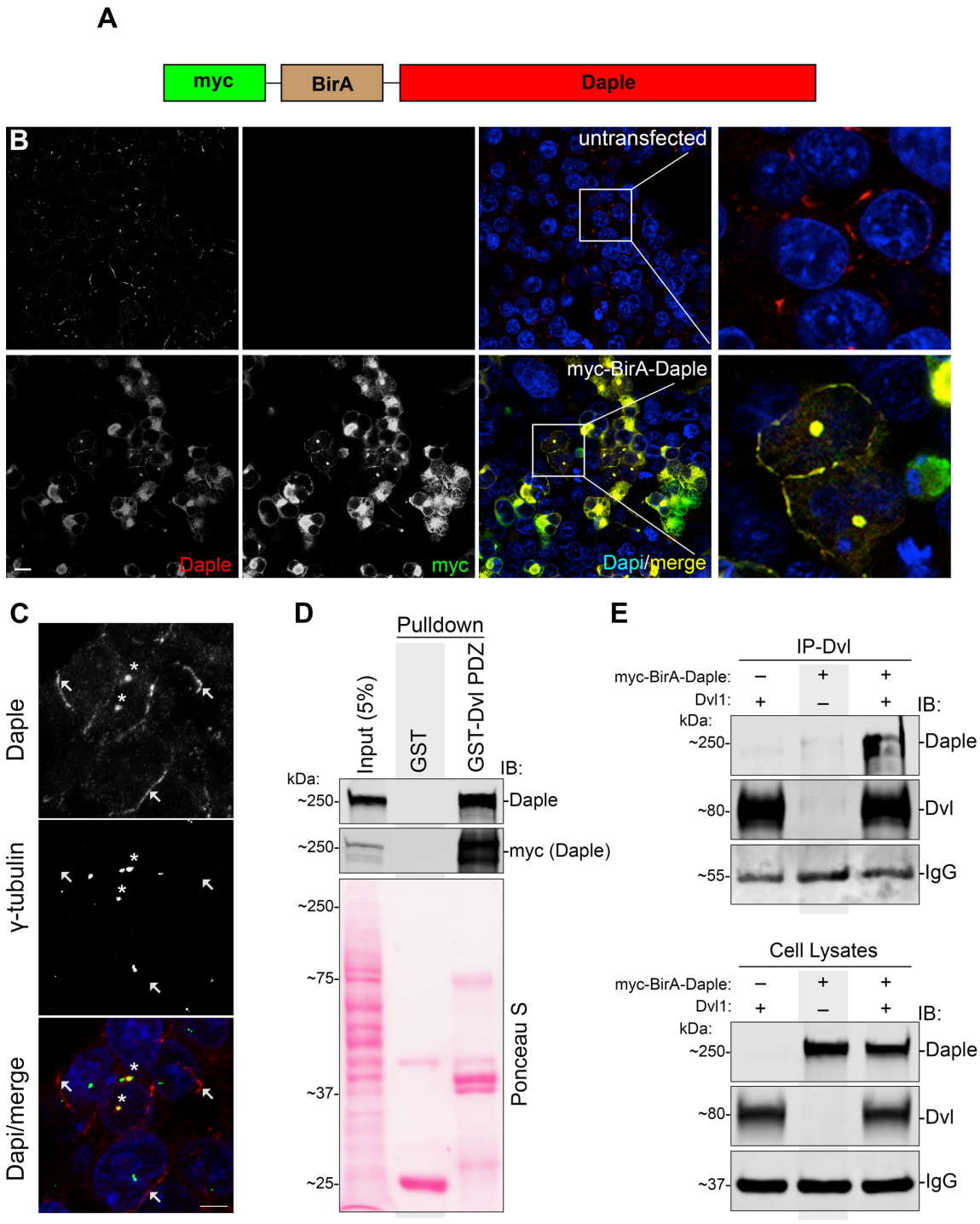

Figure S4-Related to Figure 4. Validation of the Daple construct that was used in biotin proximity labeling.

Figure S4-Related to Figure 4. Validation of the Daple construct that was used in biotin proximity labeling.

A) Schematic showing the domain composition of a myc-BirA-tagged Daple construct that was used for proximity labeling (Figure 5). **B)** HEK293T cells expressing myc-BirA-Daple were fixed and stained for Daple (*red*) or myc-tag (*green*) and analyzed by confocal microscopy. Representative images are shown. Scale bar, 25 μm. **C)** HEK293T cells were stained for endogenous Daple (red) and γ-tubulin (green). Scale bar, 5 μm. Asterisk = pericentriolar localization; arrow = PM localization. **D)** GST-pulldown assays were carried out using GST-tagged PDZ domain of Dvl and lysates of HEK293T cells with exogenously expressed myc-BirA-Daple. Immunoblots show myc-BirA-Daple bound to GST-Dvl-PDZ and confirm expression in cell lysates used in interaction assay. **E)** Co-Immunoprecipitation assays were carried out on lysates of HEK293T cells exogenously expressing myc-BirA-Daple and Dvl using anti-myc IgG or control IgG. Immunoblots show interaction of myc-BirA-Daple and Dvl in cells and confirm expression in cell lysates (input).

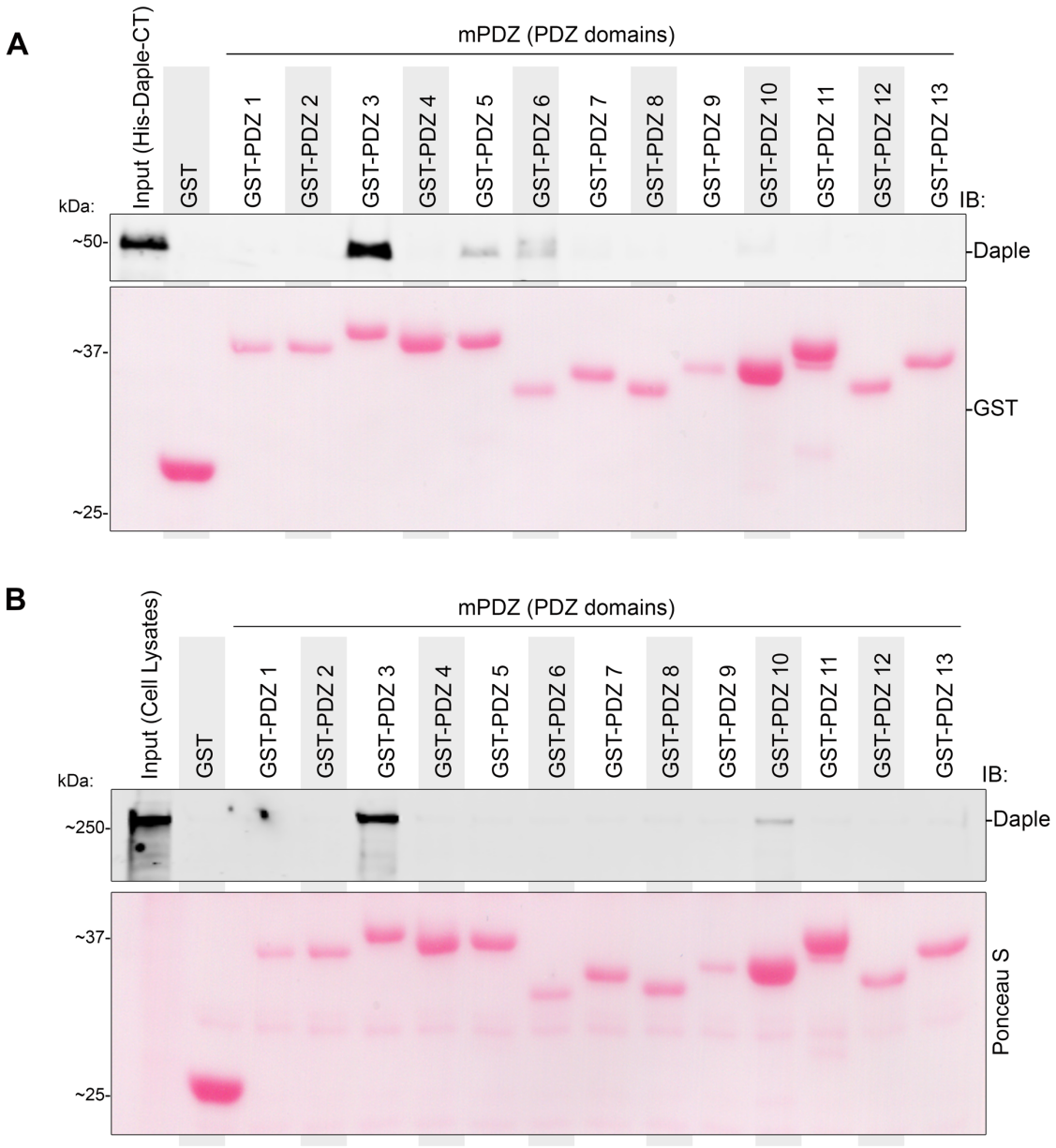

Figure S5-Related to Figure 5. Daple binds directly to mPDZ; the interaction is mediated via Daple's PBM and the third PDZ module on mPDZ.

Figure S5-Related to Figure 5. Daple binds directly to mPDZ; the interaction is mediated via Daple's PBM and the third PDZ module on mPDZ.

A) Various GST-tagged PDZ domains on mPDZ were immobilized onto glutathione S transferase beads and used in an interaction assay with recombinant His-Daple-CT. Immunoblots show interaction of purified Daple-CT with the 3rd, but not the other PDZ modules of mPDZ. **B)** mPDZ domains were bound to beads, as in (A), and used to pulldown myc-Daple from HEK293T cells. Immunoblots show bound proteins and confirm expression of Daple in cell lysates used in binding assay (input).

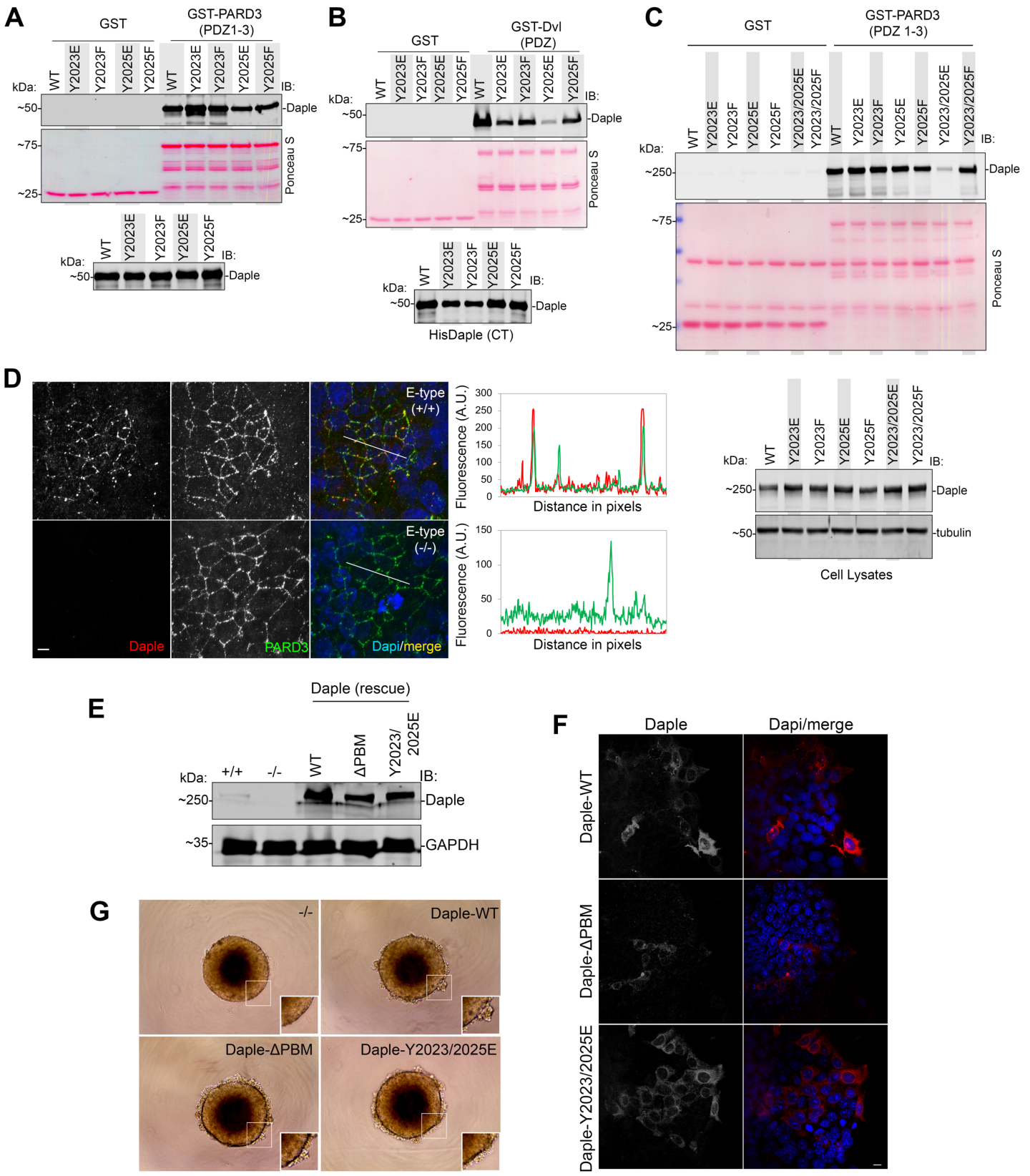

Figure S6-Related to Figure 6. Impact of Daple and its tyrosine phosphorylation on binding and localization of PARD3.

Figure S6-Related to Figure 6. Impact of Daple and its tyrosine phosphorylation on binding and localization of PARD3.

A-B) GST-tagged PDZ domain of PARD3 (A) or Dvl (B) were immobilized onto glutathione S transferase beads and used in an interaction assay with recombinant His-Daple-CT WT, Y2023E, Y2023F, Y2025E, or Y2025F. Interaction was determined through immunoblotting for Daple. **C)** GST-tagged PDZ domains of PARD3 used to pulldown ectopically expressed full length Daple-WT, Y2023E, Y2023F, Y2025E, Y2025F, Y2023/2025E, or Y2023/2025F in HEK293T cell lysates. Immunoblot for Daple show reveal loss of binding specifically in double phosphomimicking mutants. **D)** E-type (+/+) and E-type (-/-) cells were stained for Daple (*red*) and PARD3 (*green*). Scale Bar, 5μm. *Right:* RGB plot of indicated region in merge panels. **E)** Stable rescue lines of DLD1 E-type (-/-) cells expressing recombinant Daple-WT, ΔPBM, or Y2023/2025E were immunoblotted to determine expression levels. **F)** Stable lines, as described in F, were grown as spheroids as described in E and imaged on day 7. Selected regions show an inability to produce a compact spheroid and the presence of loose cells at the periphery. **G)** Stable rescue lines, as in F, were stained for Daple (red). Scale bar, 10μm.

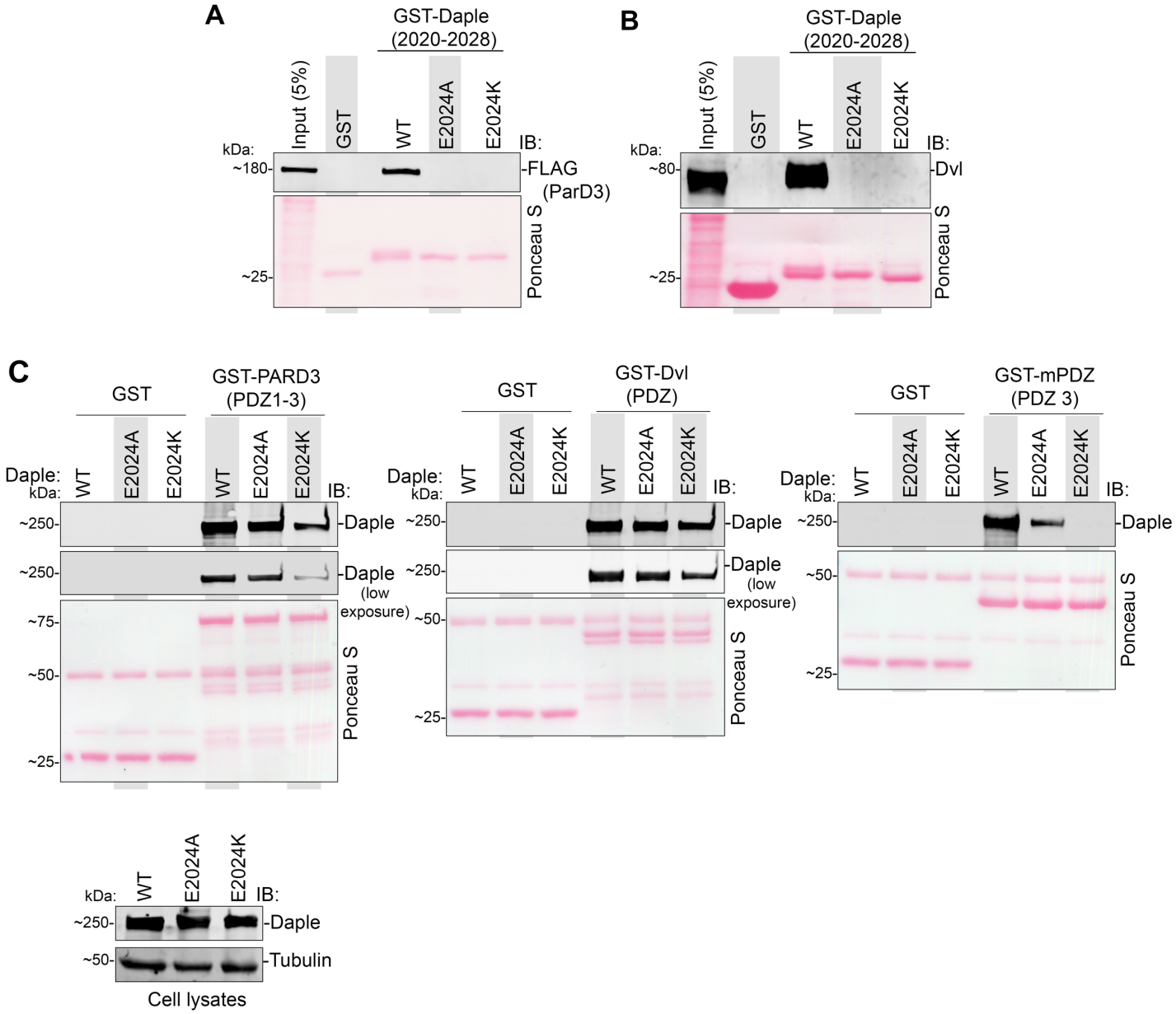

Figure S7-Related to Figure 7. Impact of E2024 on Daple's ability to bind PDZ-domain containing proteins.

Figure S7-Related to Figure 7. Impact of E2024 on Daple's ability to bind PDZ-domain containing proteins.

A-B) GST-tagged Daple-PBM-WT, E2024A, and E2024K used to pulldown full length PARD3 (A) or Dvl (B) ectopically expressed in HEK293T cells. **C)** GST-tagged PDZ domain of PARD3, Dvl, or mPDZ (PDZ3) used to pulldown ectopically expressed full length Daple-WT, E2024A, or E2024K in HEK293T cell lysates.

Transparent Methods

- KEY RESOURCE TABLE
- CONTACT FOR REAGENNT AND RESOURCE SHARING
- EXPERIMENTAL MODEL AND SUBJECT DETAILS
    - Human IHC Samples
    - Cell Lines (DLD1, CaCo-2, SW480, HEK293T, HeLa, MDCK)
    - Human Enteroids
- METHOD DETAILS
    - Cell culture and DLD1 E-type and R-type isolation
    - Isolation, expansion and culture of organoids from human colons
    - Immunofluorescence and Confocal Microscopy, Image analysis
    - Image Processing
    - Cell Fractionation
    - Immunoblotting
    - Daple CRISPR/Cas9 Gene Editing and Validation
    - Transwell Migration Assay
    - Anchorage-dependent and Anchorage-independent Colony Growth Assays
    - Measurement of trans-epithelial electrical resistance (TEER)
    - Biotin Proximity Labeling
    - In Gel Digest
    - LC-MS analysis
    - Gene Ontology analysis
    - Recombinant Protein Purification
    - In Vitro GST-Pulldown and In-cellulo Co-immunoprecipitation (CoIP) Assays
    - In Vitro Kinase Assay
    - Spheroid formation and radial migration assay on Fibronectin
    - Molecular modeling
- QUANTIFICATION AND STATISTICAL ANALYSIS
    - Statistical Analysis
    - Replications

Key Resource Table

REAGENT or RESOURCE	**SOURCE**	**IDENTIFIER**
Antibodies		
Rabbit polyclonal anti-Daple	Millipore Sigma	ABS515
Rabbit polyclonal anti-phospho Daple	21st Century Biochemicals	N/A
Rabbit polyclonal anti-Gαi3 (C-10)	Santa Cruz Biotechnology	N/A
Rabbit polyclonal anti-ZO1	GeneTex	GTX108613
Rabbit polyclonal anti-ZO1	GeneTex	GTX108627
Rabbit polyclonal anti-PARD3	Proteintech	11085-1-AP
Rabbit polyclonal anti-E-cadheren	Santa Cruz Biotechnology	sc-7870
Rabbit polyclonal anti-β-tubulin	Santa Cruz Biotechnology	sc-9104
Rabbit polyclonal anti-GM130	Cell Signaling Technology	12480S
Mouse Monoclonal anti-occludin	ThermoFisher Scientific	33-1500
Mouse monoclonal anti-β-catenin	Santa Cruz Biotechnology	sc-7963
Mouse monoclonal anti-GAPDH	Santa Cruz Biotechnology	sc-365062

Mouse monoclonal anti-αE-catenin	Santa Cruz Biotechnology	sc-9988
Mouse monoclonal anti-FLAG	Millipore Sigma	MAB3118
Mouse monoclonal anti-FLAG (hybridoma)	Purified in house	N/A
Mouse monoclonal anti-HIS	GenScript	A00186-100
Mouse monoclonal anti-GST	GenScript	A00865
Mouse monoclonal anti-Myc	Cell Signaling Technology	2276S
Mouse monoclonal anti-Myc (hybridoma)	Purified in house	N/A
Mouse monoclonal anti-phosphotyrosine	BD Biosciences	610000
Mouse monoclonal anti-Dvl	Santa Cruz Biotechnology	sc-166303
Mouse monoclonal anti-PARD3	Novus Biologicals	MAB8030
Mouse monoclonal anti-α-tubulin	Santa Cruz Biotechnology	sc-5286
Goat anti-Rabbit IgG (680)	LI-COR Biosciences	926-68071
Goat anti-Rabbit IgG, Alexa Fluor 594 conjugated	ThermoFisher Scientific	A11072
Goat anti-Mouse IgG (800)	LI-COR Biosciences	926-32210
Goat anti-Mouse IgG, Alexa Fluor 488 conjugated	ThermoFisher Scientific	A11017
Biological Samples and Cell Lines		
DLD1	ATCC	CCL-221
CaCo-2	ATCC	HTB-37
Sw480	ATCC	CCL-228
MDCK	ATCC	CCL-34
HeLa	ATCC	CCL-2
HEK293T	ATCC	CRL-11268
Colonoids (healthy normal)	HUMANOID (Human organoid research Core, UCSD)	n/a
Chemicals, Recombinant Proteins, and Plasmids		
Streptavidin, Alexa Fluor® 680 conjugate	ThermoFisher Scientific	S21378
Streptavidin, Alexa Fluor® 594 conjugate	ThermoFisher Scientific	S11227
Streptavidin Magnetic Beads	ThermoFisher Scientific	88816
Biotin	Sigma-Aldrich	B4639-500MG
DAPI (4',6-Diamidino-2-Phenylindole, Dilactate)	Thermo Fisher Scientific	D3571
Fibronectin	Thermo Fisher Scientific	PHE0023
TPA (12-O-Tetradecanoylphorbol 13-acetate, PMA, Phorbol 12-myristate 13-acetate)	Sigma-Aldrich	P1585
pSpCas9(BB)-2A-Puro (PX459) V2.0	Addgene	62988
pME-BirA	*This paper*	N/A
p3E-Daple	*This paper*	N/A
p3E-Daple-CT-WT (a.a. 1650-2028)	*This paper*	N/A
p3E-Daple-CT-ΔPBM (a.a. 1650-2025)	*This paper*	N/A
pcsDest2-BirA-Daple	*This paper*	N/A
pDEST17-Daple- CT-WT (a.a. 1650-2028)	*This paper*	N/A

pDEST17-Daple-CT-ΔPBM (a.a. 1650-2025)	*This paper*	N/A
pGEX-4T-Daple-CT-WT (a.a. 2000-2018)	*This paper*	N/A
pGEX-4T-Daple-CT-ΔPBM (a.a. 2000-2018)	*This paper*	N/A
pGEX-4T-Daple-CT-Y2023E (a.a. 2000-2018)	*This paper*	N/A
pGEX-4T-Daple-CT-Y2025E (a.a. 2000-2018)	*This paper*	N/A
pGEX-4T-Daple-CT-Y2023/2025E (a.a. 2000-2018)	*This paper*	N/A
pGEX-4T-Daple-CT-E2024A (a.a. 2000-2018)	*This paper*	N/A
pGEX-4T-Daple-CT-E2024K (a.a. 2000-2028)	*This paper*	N/A
pGEX-4T-Daple-CT-WT (a.a. 1650-2028)	Aznar, et. al., 2015	N/A
pET28b-Daple-CT-WT (a.a. 1650-2028)	Aznar, et. al., 2015	N/A
myc-pcDNA 3.1 (+) - Daple-WT (full length)	Aznar, et. al., 2015	N/A
myc-pcDNA 3.1 (+) - Daple-ΔPBM (full length)	Aznar, et. al., 2015	N/A
myc-pcDNA 3.1 (+) - Daple-FA (full length)	Aznar, et. al., 2015	N/A
myc-pcDNA 3.1 (+) - Daple-Y2025E (full length)	Aznar, et. al., 2018	N/A
myc-pcDNA 3.1 (+) - Daple-Y2025F (full length)	Aznar, et. al., 2018	N/A
myc-pcDNA 3.1 (+) - Daple-2YE (full length)	Aznar, et. al., 2018	N/A
myc-pcDNA 3.1 (+) - Daple-2YF (full length)	Aznar, et. al., 2018	N/A
pGEX-5X-1 mPDZ PDZ 1-13	Baliova M, et. al., 2014	N/A
pcDNA3.1-N-term FLAG-PARD3 (full length)	Peng Zhang, et. al., 2016	N/A
pcDNA3.1-N-term FLAG-PARD3 (ΔPDZ 1)	Peng Zhang, et. al., 2016	N/A
pcDNA3.1-N-term FLAG-PARD3 (ΔPDZ 2)	Peng Zhang, et. al., 2016	N/A
pcDNA3.1-N-term FLAG-PARD3 (ΔPDZ 3)	Peng Zhang, et. al., 2016	N/A
GST-PARD3-1N	Norimichi Itoh, et. al., 2010	N/A
GST-PARD3-2N	Norimichi Itoh, et. al., 2010	N/A
GST-PARD3-3N	Norimichi Itoh, et. al., 2010	N/A
GST-PARD3-4N	Norimichi Itoh, et. al., 2010	N/A
GST-ZO-1 PDZ 1-3	Kris Meerschaert, et. al., 2009	N/A
GST-ZO-1 PDZ 1	Kris Meerschaert, et. al., 2009	N/A
GST-ZO-1 PDZ 2	Kris Meerschaert, et. al., 2009	N/A
GST-ZO-1 PDZ 3	Kris Meerschaert, et. al., 2009	N/A
GST-ZO-2 PDZ 1	Kris Meerschaert, et. al., 2009	N/A
GST-ZO-2 PDZ 2	Kris Meerschaert, et. al., 2009	N/A
GST-ZO-2 PDZ 3	Kris Meerschaert, et. al., 2009	N/A
pGEX4T3-GIPC-PDZ	Tal Varsano, et. al., 2012	N/A
GST-mPDZ (PDZ 1 through 13)	Martina Baliova, et. al., 2014	N/A

Software		
ImageJ	National Institute of Health	https://imagej.net/Welcome
DAVID 6.8	DAVID Bioinformatics Resources	https://david.ncifcrf.gov/home.jsp
String	Snel B, et. al., 2000	string-db.org
OncoLnc	Anaya J. 2016	http://www.oncolnc.org
Molsoft ICM v3.8-6	Molsoft LLC	http://www.molsoft.com/index.html

Cell culture and DLD1 E-type and R-type isolation

All DLD1 cells were cultured using RMPI media containing 10% FBS. Cells were routinely passaged at a dilution of 1:5 to 1:10. HEK293T cells were cultured using DMEM media containing 10% FBS and routinely passaged at a dilution of 1:10.

For E-type and R-type isolation, parental stock of DLD1 cells were resuspended into single cells and plated sparsely onto 10cm tissue culture plates so that individual colonies can be picked. E-type and R-type cells can be distinguished morphologically under microscope through analyzing the amount of light passing through between cells. Further validation of proper E-type and R-type isolation was confirmed through immunoblotting for α-catenin.

Isolation, expansion and culture of organoids from human colons

Intestinal crypts were isolated from the colonic tissue specimen by digesting with Collagenase type I [2 mg/ml; Life Technologies Corporation, NY) and cultured in stem-cell enriched conditioned media with WNT 3a, R-spondin and Noggin (Mahe et al., 2015, Sato et al., 2009, Miyoshi and Stappenbeck, 2013). Briefly, after digestion with Collagenase the crypts were filtered with a cell strainer and washed with DMEM/F12 with HEPES, supplemented with 10% FBS. After adding collagenase I solution containing gentamicin (50 μg/ml, Life Technologies Corporation, NY) and mixing thoroughly, the plate was incubated at 37° C inside a CO_2 incubator for 10 min with vigorous pipetting between incubations and monitoring constantly by light microscopy to confirm by direct observation the dislodgement of the intestinal crypts from the tissues. The collagenase was inactivated with DMEM/F12 with HEPES, supplemented with 10% FBS and filtered using a 70 μm cell strainer over a 50 ml centrifuge tube. Filtered tissue was spun down at 200xg for 5 min, and the media was aspirated. The epithelial units were suspended in matrigel. Cell-matrigel suspension (15 μl) was placed at the center of the 24-well plate on ice and placed on the incubator upside-down for polymerization. After 10 min, 500 µl of 50% conditioned media (CM) was added. CM was prepared from L-WRN cells [ATCC® CRL-3276™ (Miyoshi and Stappenbeck, 2013)] with Wnt3a, R-spondin and Noggin. Y27632 (ROCK inhibitor, 10 µM) and SB431542 (an inhibitor

for TGF-β type I receptor, 10 μM) were added to the media. For human enteroids, additional supplements (purchased from Cell Applications Inc. San Diego, CA) were added to the above media. The medium was changed every 2-3 days and the enteroids were expanded as needed for experimentation.

Immunofluorescence and Confocal Microscopy, Image analysis

Cells or organoids were fixed at using -20°C methanol for 20 to 30 mins, rinse with PBS, then permeabilized for 1hr using blocking/permeabilization buffer (0.4% Triton X-100 and 2 mg/ml BSA dissolved in PBS). Primary antibody and secondary antibody were diluted in blocking buffer and incubation was carried out for 1 hr each. Coverslips were mounted using Prolong Gold (invitrogen) and imaged using a Leica SPE CTR4000 with a 63X objected and 1AU aperture. Where z-stacks was performed, images were taken at 0.5 μm slices.

Image Processing

All images were processed on ImageJ software (NIH) and assembled into figure panels using Photoshop and Illustrator (Adobe). RGB plots were generated by exporting ROI plot values and graphing into Excel (Microsoft).

Cell Fractionation

Cells expressing were harvested and suspended in homogenization buffer (10 mM sodium phosphate buffer [pH 7.2], 1 mM $MgCl_2$, 30 mM NaCl, 1 mM DTT, and 0.5 mM phenylmethylsulfonyl fluoride, supplemented with protease and phosphatase inhibitors), and homogenized using a 30-gauge needle. Crude membranes from the homogenate were pelleted by centrifugation of post-nuclear supernatant at 100,000 × *g* for 60 min at 4°C in a TLA-41 fixed-angle rotor in a TLA-100 table-top ultracentrifuge (Beckman Coulter, Krefeld, Germany). Pelleted membranes were washed in homogenization buffer before resuspension in cell lysis buffer containing 0.4% Tx-100.

Immunoblotting

For immunoblotting, protein samples were prepared in Laemmli sample buffer, separated by SDS-PAGE and transferred onto 0.4μm PVDF membrane (Millipore). After transfer, membranes were blocked with 5% Non-fat milk or 5% BSA (for phosphoprotein blotting) in PBS. Primary antibodies were prepared in blocking buffer contain 0.1% Tween-20 and incubated with blots overnight at

4°C. After primary antibody incubation, blots were incubated with secondary antibodies for one hour at room temperature and imaged using a Li-Cor Odyssey imaging system.

Daple CRISPR/Cas9 Gene Editing and Validation

Daple target genomic DNA sequence was cloned into PX-459 vector and transfected into DLD1 cells. Puromycin was added to cells 30 hours post transfection for selection. When untransfected control plates showed 95 to 100% cell death, cells were washed with PBS and fresh media (with no puromycin) was added to allow cells to recover for 8 hours. Following recovery, cells were resuspended and plated sparsely onto 10 cm plates so that individual cell colonies could be picked into 12-well plates and screened for indels.

In order to identify cell clones harboring mutations in gene coding sequence, genomic DNA was extracted using 50 mM NaOH and boiling at 95°C for 60mins. After extraction, pH was neutralized by the addition of 1.0 M Tris-pH 8.0 (10% volume). Crude genomic extract was then used in PCR reactions with primers flanking the protospacer adjacent motif (PAM) sequence. Amplicons were analyzed for indels using TBE-PAGE gels. Sequence of mutation was determined by cloning amplicons into sequencing vector using TOPO-TA cloning (Invitrogen).

Transwell Migration Assay

Transwell plates (24-well; 8.0 μm pore size; Corning) were used for chemotactic cell migration assays. Cells were trypsinized, resuspended in media containing no FBS, and placed into Transwells (200,000 cells/well). Transwells were then placed into plates containing no FBS and cells were allowed to settle for 30 mins. Inserts were then transferred into chambers containing 2% FBS overnight to trigger chemotactic migration. For fixing and staining of cells, transwells were first rinsed with PBS, then fixed using 3% paraformaldehyde in PBS for 15 mins. After fixation, transwells was rinsed with PBS, then permeabilized using 100% methanol for 15 mins, followed by rinsing in distilled water. Staining of cells were carried about by submerging transwell membrane in a 2% crystal violet solution for 30 mins, then rinse using distilled water. Non-migrated cells in upper chamber was removed using cotton swab.

Anchorage-dependent and Anchorage-independent Colony Growth Assays

Anchorage-dependent growth assays were monitored on regular tissue culture plastics. Cells were resuspended and plated at 1,000 cells per well in a 6-well plate and incubated for

approximately 10 days in 10% FBS media. Cells were then fix and permeabilized using 100% methanol. Cells were stained with 2% crystal violet and then rinsed using distilled water.

Anchorage-independent growth was performed by growing cells in a suspension of agar. A base layer of agar was prepared by dissolving 0.6% agarose in RPMI media containing 10% FBS, and then placing 3.0 ml of the solution into a 6.0 cm plate. Base layer was allowed to cool and set at room temperature for 1 hr before cell layer was added. For the cell layer, 5,000 cells were resuspended in 3.0 ml of 0.5% low melting agarose dissolved in RPMI media containing 10% FBS and then slowly placed on top of base layer with the precaution of avoiding air bubbles. Cell layer was allowed to cool and set at room temperature for 60 mins prior to transferring to 4°C for 10 mins. Plates were then placed into 37°C incubator with 5% CO_2 overnight, then 0.5 ml of RPMI media with 10% FBS was added on top and occasionally replaced to keep cells hydrated. Cells were grown for approximately 3 to 4 weeks. Cells were stained using 0.05% crystal violet dissolved in 10% ethanol. Staining solution was placed on cells for 60 mins at room temperature. Solution was then gently removed, and cells were washed several times with distilled water.

For both aforementioned colony growth assays, images were acquired by light microscopy and colonies were counted using ImageJ (NIH).

Measurement of trans-epithelial electrical resistance (TEER)

TEER of DLD1 cells was measured by culturing cells on a 0.4 μm pore size 12-mm polycarbonate Transwell Filter (Corning) followed by measurements using an epithelial voltohmmeter (Millicel-ERS resistance meter, Millipore). Cells were plated at approximately 1.5 X 10^5 cells per filter. Cells were grown for 5 days to allow for the establishment of a confluent monolayer.

Biotin Proximity Labeling

Cells were plated 24 hrs prior to transfection with Daple-BirA construct. Thirty hours post transfection, cells were incubated with 50 μM biotin for 16 hrs. Prior to lysis, cells were rinsed two times with PBS, then lysed by resuspending in lysis buffer containing (50 mM Tris, pH 7.4, 500 mM NaCl, 0.4% SDS, 1 mM dithiothreitol, 2% Triton X-100, and 1× Complete protease inhibitor) and sonication. Cell lysates were then cleared through centrifugation at 20,000 X g for 20 mins. Supernatant was then collected and incubated with Streptavidin Dynabeads overnight at 4°C. Beads were then washed twice with 2% SDS, once with wash buffer 1 (0.1% deoxycholate, 1% Triton X-100, 500 mM NaCl, 1 mM EDTA, and 50 mM HEPES, pH 7.5), followed with once wash

using wash buffer 2 (250 mM LiCl, 0.5% NP-40, 0.5% deoxycholate, 1 mM EDTA, and 10 mM Tris, pH 8.0), and once with 50mM Tris pH 8.0. Biotinylated complexes were then eluted using sample buffer containing excess biotin and heating to 100°C.

For co-immunoprecipitation of protein-protein complexes from cell lysates, cells were first lysed in cell lysis buffer (20 mM HEPES, pH 7.2, 5 mM Mg-acetate, 125 mM K-acetate, 0.4% Triton X-100, 1 mM DTT, 500 µM sodium orthovanadate, phosphatase inhibitor cocktail (Sigma-Aldrich) and protease inhibitor cocktail (Roche Life Science)) using a 28G syringe, followed by centrifugation at 10,000Xg for 10mins. Cleared supernatant was then used in binding reaction with immobilized GST-proteins for 4 hours at 4°C. After binding, bound complexes were washed four times with 1 ml phosphate wash buffer (4.3 mM Na2HPO4, 1.4 mM KH2PO4, pH 7.4, 137 mM NaCl, 2.7 mM KCl, 0.1% (v:v) Tween 20, 10 mM MgCl2, 5 mM EDTA, 2 mM DTT, 0.5 mM sodium orthovanadate). Bound proteins were then eluted through boiling at 100°C in sample buffer. Prior to mass spectrometry identification, eluted samples were run on SDS-PAGE and proteins were extracted by in gel digest.

In Gel Digest

Protein digest and mass spectrometry was perform as previously described(Shevchenko et al., 1996). The gel slices were cut to 1mm by 1 mm cubes and destained 3 times by first washing with 100 ul of 100 mM ammonium bicarbonate for 15 minutes, followed by addition of the same volume of acetonitrile (ACN) for 15 minutes. The supernatant was and samples were dried in a speedvac. Samples were then reduced by mixing with 200 µl of 100 mM ammonium bicarbonate-10 mM DTT and incubated at 56C for 30 minutes. The liquid was removed and 200 ul of 100 mM ammonium bicarbonate-55mM iodoacetamide was added to gel pieces and incubated at room temperature in the dark for 20 minutes. After the removal of the supernatant and one wash with 100 mM ammonium bicarbonate for 15 minutes, same volume of ACN was added to dehydrate the gel pieces. The solution was then removed and samples were dried in a speedvac. For digestion, enough solution of ice-cold trypsin (0.01 ug/ul) in 50 mM ammonium bicarbonate was added to cover the gel pieces and set on ice for 30 min. After complete rehydration, the excess trypsin solution was removed, replaced with fresh 50 mM ammonium bicarbonate, and left overnight at 37°C. The peptides were extracted twice by the addition of 50 µl of 0.2% formic acid and 5 % ACN and vortex mixing at room temperature for 30 min. The supernatant was removed and saved. A total of 50 µl of 50% ACN-0.2% formic acid was added to the sample, which was vortexed again at room temperature for 30 min. The supernatant was removed and combined with the

supernatant from the first extraction. The combined extractions are analyzed directly by liquid chromatography (LC) in combination with tandem mass spectroscopy (MS/MS) using electrospray ionization.

LC-MS analysis

Trypsin-digested peptides were analyzed by ultra high pressure liquid chromatography (UPLC) coupled with tandem mass spectroscopy (LC-MS/MS) using nano-spray ionization. The nanospray ionization experiments were performed using a Orbitrap fusion Lumos hybrid mass spectrometer (Thermo) interfaced with nano-scale reversed-phase UPLC (Thermo Dionex UltiMate™ 3000 RSLC nano System) using a 25 cm, 75-micron ID glass capillary packed with 1.7-µm C18 (130) BEH™ beads (Waters corporation). Peptides were eluted from the C18 column into the mass spectrometer using a linear gradient (5–80%) of ACN (Acetonitrile) at a flow rate of 375 µl/min for 1h. The buffers used to create the ACN gradient were: Buffer A (98% H_2O, 2% ACN, 0.1% formic acid) and Buffer B (100% ACN, 0.1% formic acid). Mass spectrometer parameters are as follows; an MS1 survey scan using the orbitrap detector (mass range (m/z): 400-1500 (using quadrupole isolation), 120000 resolution setting, spray voltage of 2200 V, Ion transfer tube temperature of 275 C, AGC target of 400000, and maximum injection time of 50 ms) was followed by data dependent scans (top speed for most intense ions, with charge state set to only include +2-5 ions, and 5 second exclusion time, while selecting ions with minimal intensities of 50000 at in which the collision event was carried out in the high energy collision cell (HCD Collision Energy of 30%), and the fragment masses where analyzed in the ion trap mass analyzer (With ion trap scan rate of turbo, first mass m/z was 100, AGC Target 5000 and maximum injection time of 35ms). Protein identification and label free quantification was carried out using Peaks Studio 8.5 (Bioinformatics solutions Inc.)

Gene Ontology Analysis

Identified proteins unique to plus biotin samples, but not in minus biotin samples, were analyzed using DAVID and functional annotation was grouped by INTERPRO protein domains for GO analysis. Classification with p-value less than 0.5 was set as significant.

Recombinant Protein Purification

Both GST and His-tagged proteins were expressed in E. coli stain BL21 (DE3) and purified as previously described. Briefly, cultures were induced using 1mM IPTG overnight at 25°C. Cells were then pelleted and resuspended in either GST lysis buffer (25 mM Tris-HCl, pH 7.5, 20 mM

NaCl, 1 mM EDTA, 20% (vol/vol) glycerol, 1% (vol/vol) Triton X-100, 2×protease inhibitor cocktail) or His lysis buffer (50 mM NaH_2PO_4 (pH 7.4), 300 mM NaCl, 10 mM imidazole, 1% (vol/vol) Triton X-100, 2×protease inhibitor cocktail). Cells were lysed by sonication, and lysates were cleared by centrifugation at 12,000 X g at 4°C for 30 mins. Supernatant was then affinity purified using glutathione-Sepharose 4B beads (GE Healthcare) or HisPur Cobalt Resin (Thermo Fisher Scientific), followed by elution, overnight dialysis in PBS, and then storage at -80°C.

In Vitro GST-Pulldown and In-cellulo Co-immunoprecipitation (CoIP) Assays

Purified GST-tagged proteins from E. coli were immobilized onto glutathione-Sepharose beads and incubated with binding buffer (50 mM Tris-HCl (pH 7.4), 100 mM NaCl, 0.4% (v:v) Nonidet P-40, 10 mM MgCl2, 5 mM EDTA, 2 mM DTT, 1X Complete protease inhibitor) for 60mins at room temperature. For GST-pulldown assays with recombinant proteins, the proteins were diluted in binding buffer and incubated with immobilized GST-proteins for 90mins at room temperature.

In Vitro Kinase Assays

In vitro kinase assays were performed using recombinant His-tagged Daple-CT (1650 to 2028) proteins purified from E. coli (BL21) and 50 ng of active GST-tagged recombinant Src Kinase (SignalChem, Canada). Substrates and kinase were mixed into tyrosine kinase buffer (60 mM HEPES pH 7.5, 5 mM MgCl2, 5 mM MnCl2, 3 μM sodium orthovanadate) and reaction was started by adding 1.0 mM ATP. Reactions was incubated at 25°C for 60 mins, and then used in subsequent pulldown assays or terminated using Laemmli Sample Buffer or boiling at 100°C.

Spheroid Formation and Radial Migration Assays on Fibronectin

Spheroids were produced by adding 4,000 cells into a 96-well plate precoated with 1% agarose and grown for 5 days, when well defined spheroids and necrotic core can be observed. For migration assay, the spheroids were transferred on coverslips coated with fibronectin (5 μg/ml) and the extent of radial migration was measured after 24 hrs by serial imaging of the spheroid by light microscopy. The area of migration was assessed by measuring surface area covered by cells and subtracting surface area of spheroids. Polarization towards the free-edge, and away from the tumor spheroid, was determine by the position of the Golgi towards the free-edge.

Molecular modeling

A structure of mouse PARD3 (PDZ3) with the C-terminus of mouse Cadherin-5 (QEELII, PDB 2koh (Tyler et al., 2010)), and a structure of human mPDZ (PDZ3) with the C-terminus of the PM

Ca-transporting ATPase 4 (ETSV, PDB 2iwn (Elkins et al., 2007)) were used as docking templates. The Daple PBM peptide (2021-VWYEYGCV-2028) was modeled ab initio. Although many PDZ domains recognize their target PBM peptides via a canonical anti-parallel b-sheet interaction with alternating residue backbone H-bonding pattern, this is not the case for Dvl (e.g. PDB 3cbx (Zhang et al., 2009)). Consequently, the published model of Dvl2 in complex with Daple PBM (Aznar et al., 2018) featured a kink in the peptide backbone. In this work, we explored the possibility of a similar kink in the complexes of Daple PBM with PARD3 (PDZ3) and mPDZ (PDZ3). For this, three options for H-bonding pattern between the backbones of the peptide and the target PDZ domain were tested by the modeling procedure: one skipping Daple V2028/hn bonding to Dvl I280/o (which corresponds to PARD3 V603/o and mPDZ I389/o), another skipping Daple Y2025/o and G2026/o bonding to Dvl I282/hn (which corresponds to PARD3 V605/hn and mPDZ I391/hn), and the third without H-bond skipping. For each H-bonding pattern, soft harmonic distance restraints were imposed between backbone atoms of Daple PBM peptide and the corresponding backbone atoms of the target PDZ domain. After this, the system consisting of the fully flexible peptide and the PDZ domain with flexible side-chains was thoroughly sampled using biased probability Monte Carlo sampling in internal coordinates as implemented in ICM(Abagyan and Totrov, 1994). The objective function included full-atom van der Waals term calculated using the Lennard-Jones potential and capped at 20 kcal/mol, hydrogen bonding term, electrostatics, torsional strain, and a penalty for the backbone distance restraints. Multiple poses generated by the docking procedure for each target domain were merged in a single list and rank-ordered by the predicted energy excluding the distance restraint penalty. Top-scoring conformation of each complex was selected for further analysis.

Statistical Analysis and Replicates

Graphs comparing E-type and R-type, with or without Daple, are represented as the mean ± standard error of the mean (SEM). Student's t-test was used to determine significance with P values of < 0.05 set as the threshold for statistical significance. Where statistical analysis was performed, experiments were performed in triplicates.

Supplementary References

References

ABAGYAN, R. & TOTROV, M. 1994. Biased probability Monte Carlo conformational searches and electrostatic calculations for peptides and proteins. *J Mol Biol,* 235**,** 983-1002.

ANAYA, J. 2016. OncoLnc: linking TCGA survival data to mRNAs, miRNAs, and lncRNAs. . *PeerJ Computer Science,* 2.

AZNAR, N., EAR, J., DUNKEL, Y., SUN, N., SATTERFIELD, K., HE, F., KALOGRIOPOULOS, N. A., LOPEZ-SANCHEZ, I., GHASSEMIAN, M., SAHOO, D., KUFAREVA, I. & GHOSH, P. 2018. Convergence of Wnt, growth factor, and heterotrimeric G protein signals on the guanine nucleotide exchange factor Daple. *Sci Signal,* 11.

ELKINS, J. M., PAPAGRIGORIOU, E., BERRIDGE, G., YANG, X., PHILLIPS, C., GILEADI, C., SAVITSKY, P. & DOYLE, D. A. 2007. Structure of PICK1 and other PDZ domains obtained with the help of self-binding C-terminal extensions. *Protein Sci,* 16**,** 683-94.

MAHE, M. M., SUNDARAM, N., WATSON, C. L., SHROYER, N. F. & HELMRATH, M. A. 2015. Establishment of human epithelial enteroids and colonoids from whole tissue and biopsy. *J Vis Exp*.

MIYOSHI, H. & STAPPENBECK, T. S. 2013. In vitro expansion and genetic modification of gastrointestinal stem cells in spheroid culture. *Nat Protoc,* 8**,** 2471-82.

SATO, T., VRIES, R. G., SNIPPERT, H. J., VAN DE WETERING, M., BARKER, N., STANGE, D. E., VAN ES, J. H., ABO, A., KUJALA, P., PETERS, P. J. & CLEVERS, H. 2009. Single Lgr5 stem cells build crypt-villus structures in vitro without a mesenchymal niche. *Nature,* 459**,** 262-5.

SHEVCHENKO, A., WILM, M., VORM, O. & MANN, M. 1996. Mass spectrometric sequencing of proteins silver-stained polyacrylamide gels. *Anal Chem,* 68**,** 850-8.

TYLER, R. C., PETERSON, F. C. & VOLKMAN, B. F. 2010. Distal interactions within the par3-VE-cadherin complex. *Biochemistry,* 49**,** 951-7.

ZHANG, Y., APPLETON, B. A., WIESMANN, C., LAU, T., COSTA, M., HANNOUSH, R. N. & SIDHU, S. S. 2009. Inhibition of Wnt signaling by Dishevelled PDZ peptides. *Nat Chem Biol,* 5**,** 217-9.